Mantle Heterogeneity and Melting Processes in the South China Sea: Thermal and Melting Models Constrained by Oceanic Crustal Thickness and Basalt Geochemistry

Xubo Zhang[1,2,3,4,5] , Jian Lin[1,2,3,5,6] , and Mark D. Behn[5,7]

[1]Key Laboratory of Ocean and Marginal Sea Geology, South China Sea Institute of Oceanology, Innovation Academy of South China Sea Ecology and Environmental Engineering, Chinese Academy of Sciences, Guangzhou, China, [2]Southern Marine Science and Engineering, Guangdong Laboratory (Guangzhou), Guangzhou, China, [3]China-Pakistan Joint Research Center on Earth Sciences, CAS-HEC, Islamabad, Pakistan, [4]State Key Laboratory of Marine Geology, School of Ocean and Earth Science, Tongji University, Shanghai, China, [5]Department of Geology and Geophysics, Woods Hole Oceanographic Institution, Woods Hole, MA, USA, [6]Department of Ocean Science and Engineering, Southern University of Science and Technology, Shenzhen, China, [7]Department of Earth and Environmental Sciences, Boston College, Chestnut Hill, MA, USA

Abstract We simulate mantle flow, thermal structure, and melting processes beneath the ridge axis of the South China Sea (SCS), combining the nominally anhydrous melting and fractional crystallization model, to study mantle heterogeneity and basin evolution. The model results are constrained by seismically determined crustal thickness and major element composition of fossil ridge axis basalts. The effects of half-spreading rate, mantle potential temperature, mantle source composition, and the pattern of melt migration on the crustal thickness and magma chemical composition are systematically investigated. For the SCS, the east and southwest (SW) subbasins have comparable crustal thickness, but the east subbasin has higher FeO and Na_2O contents compared to the SW subbasin. The estimated best fitting mantle potential temperatures in the east and SW subbasins are 1,360 ± 15 °C and 1,350 ± 25 °C, respectively. The mantle in the east subbasin (site U1431) prior to the cessation of seafloor spreading is composed primarily of the depleted mid-ocean ridge basalt mantle (DMM), and is slightly contaminated by eclogite/pyroxenite-rich component. However, the mantle source composition of the SW subbasin (sites U1433 and U1434) contains a small percentage (2–5%) of lower continental crust. Basalt samples at the northern margin of the east subbasin (site U1500) shows similar chemical characteristics with that of the SW subbasin. We suggest that the basin-scale variability in the mantle heterogeneity of the SCS can be explained by a single model in which the contamination by the lower continental crust is gradually diluted by melting of DMM as the ridge moves away from the rifted margin.

1. Introduction

The South China Sea (SCS) is one of the largest marginal seas in the western Pacific and is located at the junction of the Eurasian, Philippine Sea, and Indo-Australian plates (Figure 1). The SCS can be divided into the northwest subbasin, east subbasin, and SW subbasin. Despite its relatively short evolution history, the SCS has undergone a series of tectonic and magmatic processes, including continental rifting and breakup, seafloor spreading, and subduction, together with extensive magmatism (e.g., Briais et al., 1993; Ding et al., 2018; Li et al., 2015; Pautot et al., 1990; Sibuet et al., 2016; Taylor & Hayes, 1980, 1983; Tu et al., 1992; Yan et al., 2014; Zhao et al., 2019). The tectonic and mantle evolution in the SCS is also strongly affected by surrounding subduction zones (e.g., Lin et al., 2019; Sun et al., 2019; Wang et al., 2019). Contrary to the classical magma-poor margin, the SCS experiences fast lithospheric extension, rapid magmatism, and fast transition from continental breakup to seafloor spreading without direct evidence of mantle exhumation (Larsen et al., 2018).

Seafloor spreading in the SCS occurred during the Oligocene to mid-Miocene (Briais et al., 1993; Li et al., 2014; Taylor & Hayes, 1980, 1983). Based on analyses of magnetic anomaly data, Taylor and Hayes (1980, 1983) and Briais et al. (1993) suggested that the age of the SCS is from ~30 to 16 Ma according to the latest geomagnetic polarity timescale (Cande & Kent, 1995; Ogg, 2012). A southward ridge jump occurred after the magnetic anomaly C7, accompanied by seafloor spreading that propagated toward the southwest
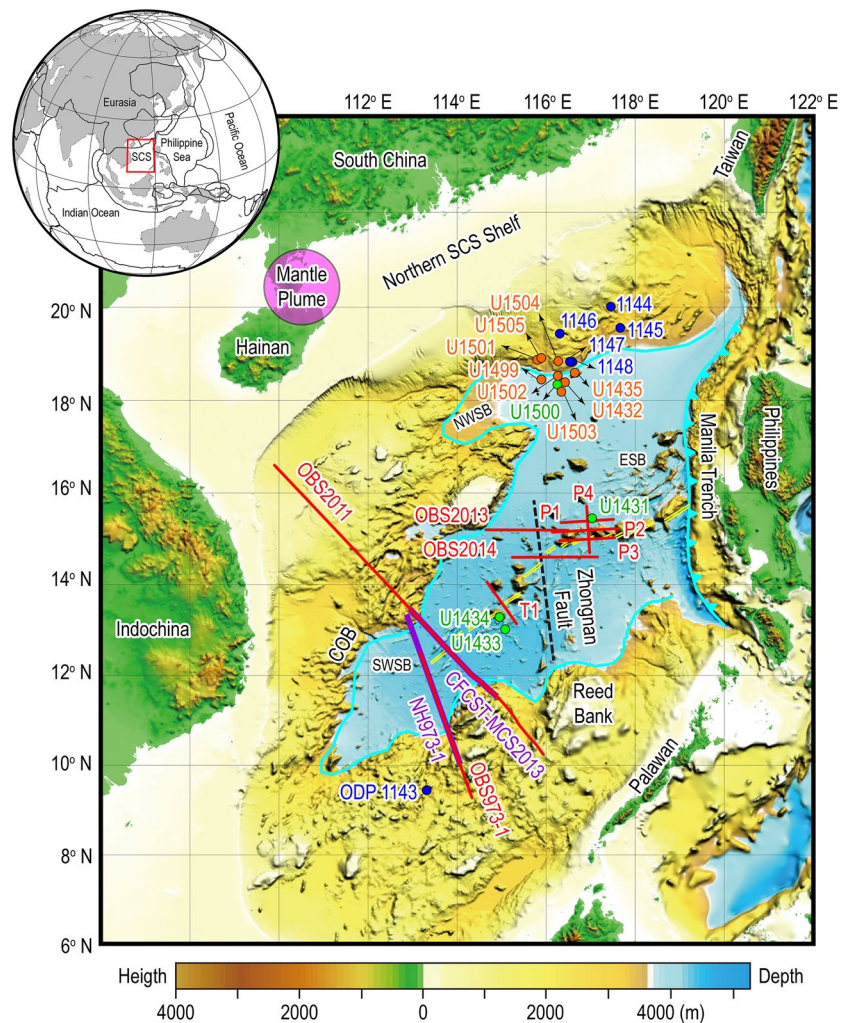
Figure 1. Tectonic location and bathymetric map of the South China Sea (SCS). The orange and purple solid lines represent seismic profiles, which include P1, P2, P3, and P4 (Zhao et al., 2018), OBS2013 and OBS2014 (Ruan et al., 2016), T1 (Zhang et al., 2016), CFCST-MCS2013 and NH973-1 (Yu et al., 2018a), OBS2011 (Pichot et al., 2014), and OBS973-1 (Qiu et al., 2011). Blue dots mark locations of ODP Expedition 184 sites (sites 1143, 1144, 1145, 1146, 1147, and 1148). Orange and green dots mark locations of IODP Expedition 349 (U1431, U1432, U1433, U1434, and U1435), 367 (U1499 and U1500), 368 (U1501, U1502, U1503, U1504, and U1505), and 368X sites (U1503 A). The double yellow dashed line represents the fossil spreading ridge (Briais et al., 1993). The cyan solid line represents the continent-ocean boundary (COB) and the cyan solid line with triangles indicates the Manila trench. The location of Zhongnan fault (black dashed line) is modified from Li et al. (2015). The location of Hainan mantle plume (purple shaded region) is modified from Wei and Chen (2016). The bathymetric map is modified from Yang et al. (2015). NWSB: northwest subbasin, ESB: east subbasin, SWSB: southwest subbasin.

(Briais et al., 1993). Through analyzing high-resolution deep-tow magnetic data and the results of International Ocean Discovery Program (IODP) Expedition 349, Li et al. (2014) proposed that the opening age of the SCS is ∼33 Ma, and the cessation ages of the east and SW subbasin are ∼15 and 16 Ma, respectively. Post-spreading volcanism is widely distributed in the SCS, including a seamount chain along the fossil spreading axis (Wang et al., 1985; Tu et al., 1992; Yan et al., 2008a, 2008b, 2014, 2015).

Extensive seismic surveys, including multichannel seismic (MCS) and ocean bottom seismometer (OBS), have been carried out over the continental margins and oceanic subbasins, with several seismic profiles crossing the fossil spreading ridges (e.g., Pichot et al., 2014; Qiu et al., 2011; Ruan et al., 2016; Yu et al., 2017; Yu et al., 2018a; Zhang et al., 2016; Zhao et al., 2018). Postspreading volcanism has modified the crustal thickness near the fossil spreading ridges (Zhang et al., 2016; Zhao et al., 2018). In the east subbasin, an

80-km-wide zone with relative thin crust (<5 km) was formed along the fossil spreading ridge, which might be attributed to a decrease in spreading rate prior to the cessation of seafloor spreading (Zhao et al., 2018). Due to overall southwestward ridge propagation in the SW subbasin, tectonic features of different spreading stages are observed, ranging from mature spreading at the northwest segment to initial spreading at the southwest segment (Li et al., 2012). The combined analyses of gravity and seismic data reveal systematically thicker crust on the northern flank of fossil spreading ridge in the SCS subbasins than the southern conjugate, which is interpreted to reflect higher mantle temperature and/or more enriched mantle source beneath the northern flank (Zhang et al., 2018a).

Recent geophysical and geochemical studies have revealed mantle anomalies underneath the Hainan Island region, leading to the hypothesis of a Hainan mantle plume (Fan & Menzies, 1992; Huang, 2014; Wei & Chen, 2016; Xu et al., 2012; Yan et al., 2008b, 2015, 2008a; Yan & Shi, 2007; Yu et al., 2018a; Zhang et al., 2018b). Seismic modeling shows that the mantle transition zone beneath the Hainan Island and Leizhou Peninsula is thinner than the global average (Wei & Chen, 2016). It is proposed that the Hainan plume may have triggered the opening of the SCS (Yan et al., 2014; Yan & Shi, 2007). The Hainan plume might have impinged on the lithosphere of the SCS continental margin in the mid-Oligocene and promoted the ridge jump and propagation in the SCS (Yu et al., 2018b). Sr-Nd-Pb-Hf isotopic ratios reveal complex mantle source compositions beneath the SCS subbasins, including the contamination by a small amount of lower continental crust (LCC) in the SW subbasin (Zhang et al., 2018b).

In this study, we construct two-dimensional (2-D) models to simulate mantle flow, thermal structure, and melting processes of the SCS and to reveal mantle heterogeneity. The simulated mantle flow and thermal structure are combined with the mantle melting model of Behn and Grove (2015) and fractional crystallization model of Yang et al. (1996) to calculate the predicted crustal thickness and lava composition at the SCS spreading axis. The dependence of the predicted crustal thickness and lava composition on half-spreading rate U, mantle potential temperature T_p, mantle source composition, and melt pooling width W_{pool} is investigated. We then discuss the implications of the observed mantle heterogeneity on mantle evolution and melting processes in the SCS.

2. Data Constraints

2.1. Major and Trace Element Contents of Basalts

Several IDOP Expeditions (IODP 349, 367, 368, and 368X) had been conducted in the SCS in recent years (Figure 1). The igneous oceanic crust near fossil spreading ridges was first sampled by IODP Expedition 349 at site U1431 in the east subbasin and sites U1433 and U1434 in the SW subbasin (Expedition 349 Scientists, 2014). At the northern margin of the east subbasin, mid-ocean ridge basalt (MORB) samples were recovered at sites U1500 and U1502 by IODP Expeditions 367/368 (Jian et al., 2018; Sun et al., 2018), and at site U1503 by IODP Expedition 368X (Childress et al., 2019). These drilling expeditions form a transect crossing the continent-ocean boundary (COB) (Figure 1).

Basalt samples of site U1431 have comparable major element contents with global MORBs except for relatively lower CaO content (Figure S1). Most basalt samples of site U1431 have higher MgO content compared to sites U1433 and U1434 in the SW subbasin. For a given MgO content, basalt samples of site U1431 have relatively higher FeO and Na$_2$O contents, and lower CaO content (Figure S1). Rare Earth elements (REEs) show that most samples of site U1431 are similar to normal mid-ocean ridge basalt (N-MORB) and a few are similar to enriched mid-ocean ridge basalt (E-MORB); meanwhile basalt samples of sites U1433 and U1434 are similar to E-MORB (Figures S2a and S2b).

The basalt samples of sites U1500, U1502, and U1503 around the northern COB in the east subbasin are crucial to understand the mantle evolution from continental breakup to initial seafloor spreading. Site U1502 was flooded by remnants of continental lithosphere, which recorded the magmatism during the final stage of continental rifting and breakup (Larsen et al., 2018). Sites U1500 and U1503 sampled the oceanic crust formed during the incipient seafloor spreading (Childress et al., 2019; Yu & Liu, 2020). The bulk-rock major and trace element contents of site U1500 are selected from Yu and Liu (2020). Major element contents of site U1500 are consistent with that of sites U1433 and U1434 in the SW subbasin (Figure S1). The REE pattern

of site U1500 is similar to E-MORB (Figure S2c). The postcruise geochemistry data of U1500 and U1503 have not yet been released (Childress et al., 2019). In this study, the numerical model results are mainly constrained by MORBs of sites U1431, U1433, and U1434 near fossil spreading ridges.

2.2. Seismically Determined Crustal Thickness

In the east subbasin, four seismic profiles (P1, P2, P3, and P4) are selected to estimate crustal thickness near the fossil spreading ridge (Figure 1). The segments cutting across seamounts or the continental crust are excluded (Figure S3). Profiles P1, P2, and P3 are parallel to the Zhenbei-Huangyan seamounts chain, while profile P4 is perpendicular to the seamounts chain. Profile P1 is located north of the fossil spreading ridge in the east subbasin. The crustal thickness along profile P1 is not influenced by postspreading magmatism, and varies from 4.8 to 6.3 km (Figure S3a; Zhao et al., 2018). The part of profile P2 between two seamounts has crustal thickness of 5–6 km (Figure S3b; Zhao et al., 2018). Profile P3 is located south of profile P1, and has crustal thickness of 3.5–6 km except for its western extremity across the Zhenbei seamount (Figure S3c; Zhao et al., 2018). The thinner crust (<5 km) is observed along the western portion of profile P3. Profile P4 has a crustal thickness of 3.7–6.4 km excluding the southern segment crossing the Jixiang seamount (Figure S3d; Zhao et al., 2018). The thinner crust (<5 km) is limited to the southern segment of profile P4. A narrow zone with thinner crust (<5 km) is located along the fossil spreading ridge in the east subbasin; the outside of which has normal crustal thickness of 5–6 km except at seamounts (Zhao et al., 2018). Site U1431 is located near the northern edge of this thinner crustal zone (Zhao et al., 2018) and is close to profile P1.

In the SW sub-basin, five seismic profiles (T1, OBS2011, OBS973-1, CFCST-MCS2013, and NH973-1) are selected to estimate crustal thickness (Figure 1). Profile T1 is perpendicular to the fossil spreading ridge in the SW subbasin, and is located close to IODP sites U1433 and U1434. The crustal thickness along Profile T1 is 6–7 km and is likely thickened by postspreading magmatism, except for a narrow region of thin crust (<5 km) associated with detachment faulting north of the fossil spreading ridge (Figure S3e; Zhang et al., 2016). Profiles OBS2011 and OBS973-1 crossing the fossil spreading ridge are located away from regions modified by postspreading magmatism. The crustal thickness along OBS2011 varies from 5.1 to 5.8 km (Figure S3f; Pichot et al., 2014). Profile OBS973-1 has crustal thickness of 4–6.3 km, except for the thinner crust (<4 km) at the central axial valley (Figure S3h; Qiu et al., 2011). The average crustal thickness along profile OBS973-1 is 5.3 km (Yu et al., 2017), which is consistent with the result of Qiu et al. (2011). However, the crustal thickness inferred from MCS profiles CFCST-MCS2013 and NH973-1 is only 1.5–3.6 km (Figures S3g and S3i; Yu et al., 2018a), which is much thinner than that derived from profiles OBS2011 (Pichot et al., 2014) and OBS973-1 (Qiu et al., 2011). The Moho discontinuity identified along the MCS profiles, defined as a wave impedance boundary between the oceanic crust and uppermost mantle, is not very clear or continuous (Yu et al., 2018a). Thus, we use the velocity model derived from OBS profiles to constrain the crustal thickness in the SW subbasin. The crustal thickness beneath sites U1433 and U1434 is mainly constrained by profiles OBS973-1, which is not modified by postspreading volcanism.

2.3. Half-Spreading Rates

The half-spreading rate model in the SCS is constrained by the relatively high-resolution deep-tow magnetic anomalies and the results of IODP Expedition 349. The east subbasin has a half-spreading rate of 1–4 cm/yr, while the SW subbasin has a half-spreading rate of 2 cm/yr (Li et al., 2014). Since basalt samples (sites U1431, U1433, and U1434) used in the study are close to spreading ridges (Figure 1), we focus on the half-spreading rate variations during the period of a few million years before seafloor spreading stopping. The half-spreading rates are 1.8–2.3 and 2 cm/yr in the east and southwest subbasins prior to the cessation of seafloor spreading, respectively (Table S1).

3. Numerical Models

To estimate mantle potential temperature and mantle source composition beneath the SCS subbasins, a 2-D model is combined with a mantle melting model to simulate mantle upwelling and decompression melting processes. First, the COMSOL Multiphysics 5.0 is used to calculate mantle flow and temperature. Then the melt fraction and melt composition at each melting step are determined by the melting model of Behn and Grove (2005). The resultant melt is assumed to rise vertically through the mantle column until it encounters a permeability barrier (e.g., top of the melting region, base of the lithosphere, clinopyroxene-out reaction zone), and then migrates laterally along this boundary to the ridge axis (Ghods & Arkani-Hamed, 2000; Kelemen & Aharanov, 1998; Magde et al. 1997; Magde & Sparks, 1997; Sparks et al., 1993; Sparks & Parmentier, 1991). Prior to eruption, the aggregate melt beneath the ridge axis undergoes fractional crystallization due to the cooling effect of the shallow mantle lithosphere, which is modeled using the approach of Yang et al. (1996).

3.1. Mantle Flow and Temperature

The 2-D models of mantle flow and thermal structure beneath a spreading ridge are calculated using the finite-element software package COMSOL Multiphysics 5.0, assuming a visco-plastic rheology (Figures 2 and 3). COMSOL Multiphysics has been successfully used for simulation of mantle flow and temperature in geologic systems (Behn et al., 2007, 2015; Georgen et al., 2014, 2011; Gregg et al., 2009; Montési et al., 2011; van Keken et al., 2008). Mantle flow is driven by the divergence of two surface plates moving apart at a half-spreading rate U of 0.5–10 cm/yr (Figure 2a). The vertical sides and bottom boundary of the model domain are set as open boundaries with normal stress set to be the lithostatic pressure. The top and bottom temperature boundaries are set as Dirichlet boundary conditions (i.e., fixed temperature boundaries). The surface temperature is set to $T_s = 0$ °C. The mantle potential temperature (T_p) is assumed to vary between 1,300 and 1,450 °C. The bottom temperature (T_m) of the model domain is determined by extrapolating the mantle potential temperature along an adiabat with gradient of 1.5 °C/kbar to the base of the model (i.e., 100 km). The vertical sides of the model domain are set as insulated walls. Model parameters are given in Table 1.

The conservation of mass, momentum, and energy are given, respectively, by

$$\nabla \cdot \boldsymbol{u} = 0 \tag{1}$$

$$-\nabla \cdot \left[\eta_{eff} \left(\nabla \boldsymbol{u} + \nabla \boldsymbol{u}^T \right) \right] + \nabla p = \rho \boldsymbol{g} \tag{2}$$

$$\rho C_p \boldsymbol{u} \cdot \nabla T - k \nabla^2 T = 0 \tag{3}$$

where $\boldsymbol{u}$ is velocity, p is total pressure, η_{eff} is effective mantle viscosity, ρ is mantle density, $\boldsymbol{g}$ is gravitational acceleration, C_p is specific heat capacity, T is temperature, and k is thermal conductivity. Bold denotes a vector quantity.

A visco-plastic mantle rheology is assumed, which incorporates brittle weakening within the lithosphere (Behn et al., 2007; Chen & Morgan, 1990). Compared to the model of a constant or temperature-dependent viscosity, the visco-plastic viscosity model promotes enhanced upwelling directly beneath the ridge axis, thus resulting in a warmer thermal structure and more melting (Figure S4; Behn et al., 2007, 2015;Gregg et al., 2009; Montési et al., 2011; Roland et al., 2010). The effective mantle viscosity is defined by (Behn et al., 2007; Gregg et al., 2009)

$$\eta_{eff} = \left(\frac{1}{\eta_{td}} + \frac{1}{\eta_{byr}} + \frac{1}{\eta_{max}} \right)^{-1} \tag{4}$$
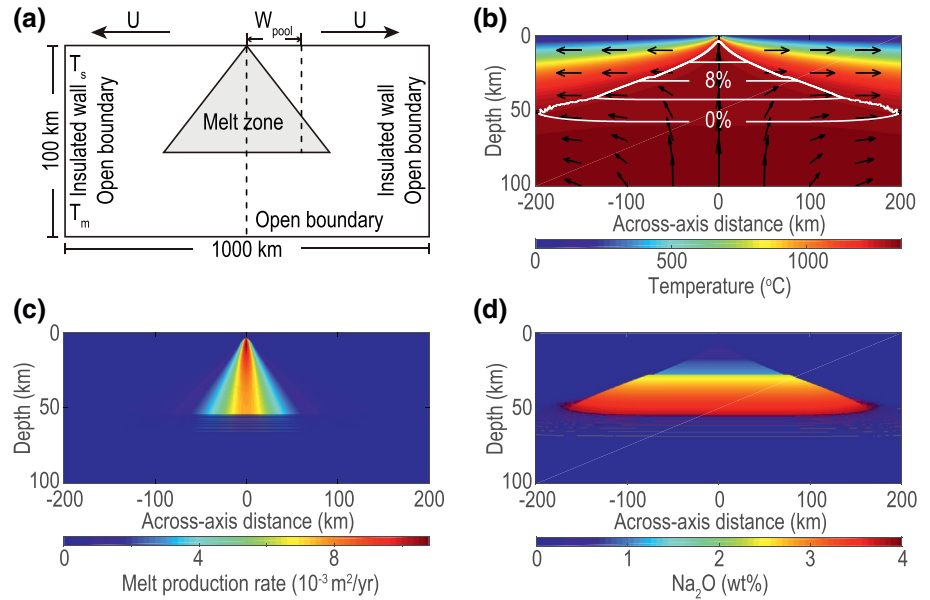
Figure 2. Two-dimensional spreading ridge model and resultant model result. (a) Model geometry and boundary conditions. Model parameters include half-spreading rate, U; mantle temperature at the surface, T_s, and at the base of the model, T_m; and the melt pooing width, W_{pool}. The light gray triangle illustrates the melt zone. (b) Modeled mantle flow (black arrows), temperature (background color), and melt fraction (white contours). The number with white color represents melting degree. (c) Melt production rate. (d) Na_2O content of the incremental melt. The half-spreading rate of 2 cm/yr, mantle potential temperature of 1,350 °C, and the depleted MORB mantle (Workman & Hart, 2005) are assumed for the simulation.

where η_{td} is temperature-dependent viscosity, η_{byr} is a brittle strength approximation based on Byerlee's law, and η_{max} is an assumed maximum viscosity (10^{23} Pa s).

The temperature-dependent viscosity is calculated by (Gregg et al., 2009)

$$\eta_{td} = \eta_0 \exp\left(\frac{Q}{R}\left(\frac{1}{T} - \frac{1}{T_m}\right)\right) \tag{5}$$

where η_0 is reference viscosity (10^{19} Pa·s), Q is activation energy, R is universal gas constant, and T_m is the mantle temperature at the model base.

The viscosity associated with brittle failure is approximated by (Behn et al., 2007; Chen & Morgan, 1990; van Keken et al., 2008)

$$\eta_{byr} = \frac{\tau_{\max}}{2\dot{\varepsilon}_{||}} \tag{6}$$

where τ_{max} is maximum shear stress that the lithosphere can sustain,

$$\tau_{\max} = C_0 + \mu\rho gz \tag{7}$$

and $\dot{\varepsilon}_{//}$ is second invariant of the strain rate tensor:

$$\dot{\varepsilon}_{||} = \left[\frac{1}{2}\sum_{ij}\dot{\varepsilon}_{ij}\dot{\varepsilon}_{ij}\right]^{\frac{1}{2}} \tag{8}$$
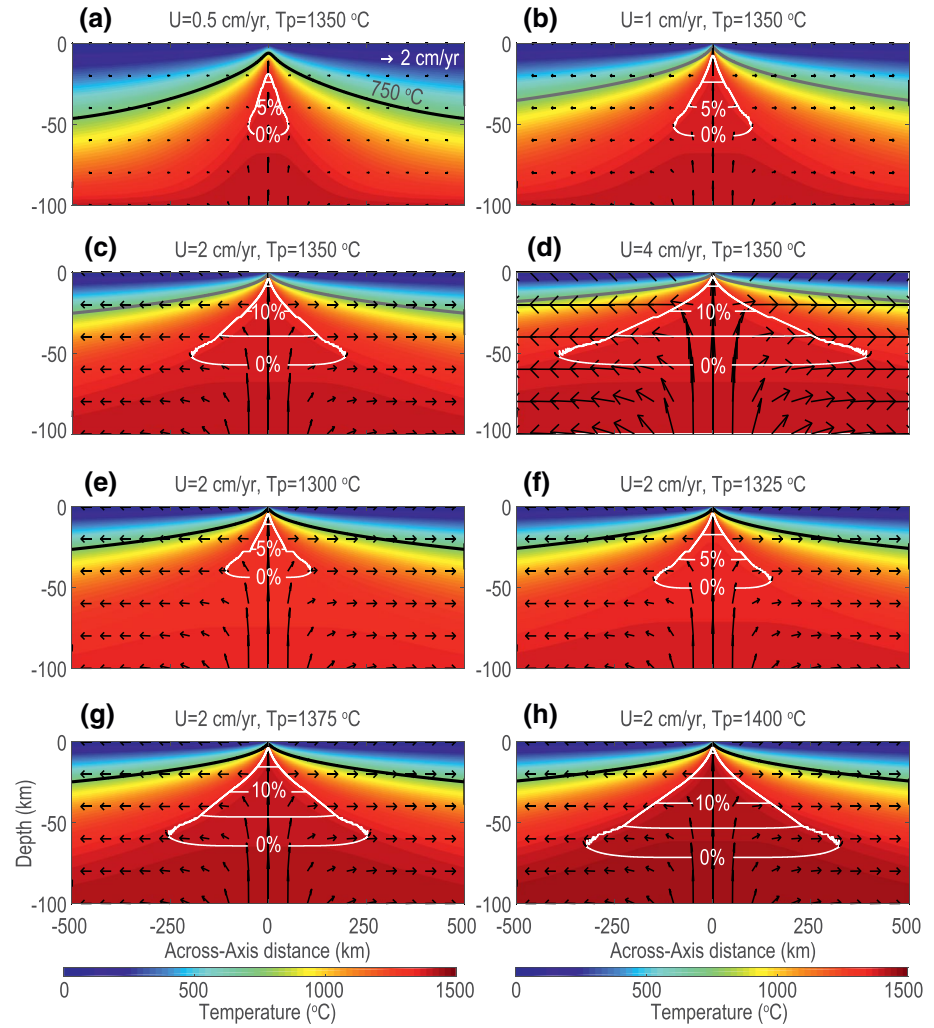
Figure 3. Comparison of mantle flow, temperature, and melt fraction for models with different half-spreading rates and mantle potential temperatures. The black arrows represent mantle flow and white contours represent the melt fraction. The black contour marks the 750 °C isotherm, which indicates the bottom of oceanic lithosphere. The input mantle source composition is set as the depleted MORB mantle (Workman & Hart, 2005).

Here C_0 is cohesion (10^7 Pa), μ is friction coefficient (0.6), g is gravitational acceleration, z is depth, and $\dot{\varepsilon}_{ij}$ is the component of the strain rate tensor,

$$\dot{\varepsilon}_{ij} = \frac{1}{2}\left[\frac{\partial u_i}{\partial j} + \frac{\partial u_j}{\partial i}\right] \tag{9}$$

where u_i and u_j are components of the velocity vector $\boldsymbol{u}$.

3.2. Melt Generation, Migration, and Extraction

The melting process beneath the spreading ridges is assumed to be adiabatic and is dependent on temperature, pressure, and mantle composition (Asimow & Langmuir, 2003; Grove et al., 1992; Klein & Langmuir, 1987; Langmuir et al., 1992). The variations in lava composition and crustal thickness along global mid-ocean ridge segments can be explained by models with polybaric, anhydrous melting of peridotite (e.g., Asimow et al., 2001; Behn & Grove, 2015). The water in the mantle source also plays an important role in mantle melting. The addition of water to the source can lower the mantle solidus and cause melting to begin

Table 1
Model Parameters

Parameter	Description	Value
ρ_m	Mantle density (kg m^{-3})	3,300
η_0	Reference viscosity (Pa s)	10^{19}
η_{max}	Maximum viscosity (Pa s)	10^{23}
C_p	Specific heat capacity (J Kg^{-1} K^{-1})	1,250
k	Thermal conductivity (W m^{-1} K^{-1})	3
Q	Activation energy (J mol^{-1})	$2.5 * 10^5$
R	Universal gas constant (J mol^{-1} K^{-1})	8.3114
T_s	Temperature at the surface of the model domain (°C)	0
T_p	Mantle potential temperature (°C)	1,300–1,450
U	Half-spreading rate (cm yr^{-1})	0.5–10
g	Gravitational acceleration (m s^{-2})	9.8
C_0	Cohesion (Pa)	10^7
μ	Friction coefficient	0.6
L	Latent heat of melting (J Kg^{-1})	$4 * 10^5$

at a greater depth compared to anhydrous melting (Asimow et al., 2004; Asimow & Langmuir, 2003; Katz et al., 2003).

We utilize the mantle melting model of Behn and Grove (2015) (hereafter referred to as BG15) to calculate melt fraction and composition. The BG15 model is a nominally anhydrous melting model in the plagioclase-spinel fields, in which melting is parameterized as a function of temperature, pressure, and mantle composition. The BG15 model does not explicitly consider variations in mantle solidus associated with changes in composition. Combined with fractional crystallization model of Yang et al. (1996), the above model has successfully reproduced the crustal thickness and MORBs geochemistry of global mid-ocean ridge systems (Behn & Grove, 2015). The melting calculation is done as a postprocessing step and thus did not influence the mantle flow and temperature simulation.

We assume polybaric incremental batch melting and a constant melt productivity of 1% kbar^{-1} in the model (Behn & Grove, 2015; Gregg et al., 2009). As the mantle moves upward, 90% of the generated melt at each melting step is removed and accumulated at the ridge axis, while the remaining melt and depleted mantle residue continue to ascend and undergo further melting (Ahern & Turcotte, 1979; Behn & Grove, 2015; Gregg et al., 2009). The calculation of the composition of the lava that aggregated beneath the ridge axis consists of the following three steps (Behn & Grove, 2015; Gregg et al., 2009): (1) The composition of the melt at every model grid is calculated using the BG15 melting model. (2) The resultant melt is assumed to move upward through the mantle column until it reaches the top of the melting zone, and then migrates laterally and pools beneath the ridge axis. (3) Prior to extraction, the melt pooled at the ridge axis undergoes fractional crystallization due to mantle cooling. The mantle lithology is assumed as spinel lherzolite (Behn & Grove, 2015; Gregg et al., 2009; Workman & Hart, 2005). Models with different input mantle source compositions are used to predict the influence of source variability on lava composition (Figure 4). The major element compositions of end-member sources used in the study are given in Table 2.

3.2.1. Melt Generation

The BG15 model (Behn & Grove, 2015) is developed from the fractional melting model of Kinzler and Grove (1992a, 1992b, 1993, 1997), but incorporates new experimental data (Till et al., 2012). Using the BG15 model, we track the major element compositions of the residual mantle and resultant melt (SiO$_2$, TiO$_2$, Al$_2$O$_3$, Cr$_2$O$_3$, FeO, MgO, CaO, K$_2$O, and Na$_2$O) at each melting step. We also track changes in mantle solidus and
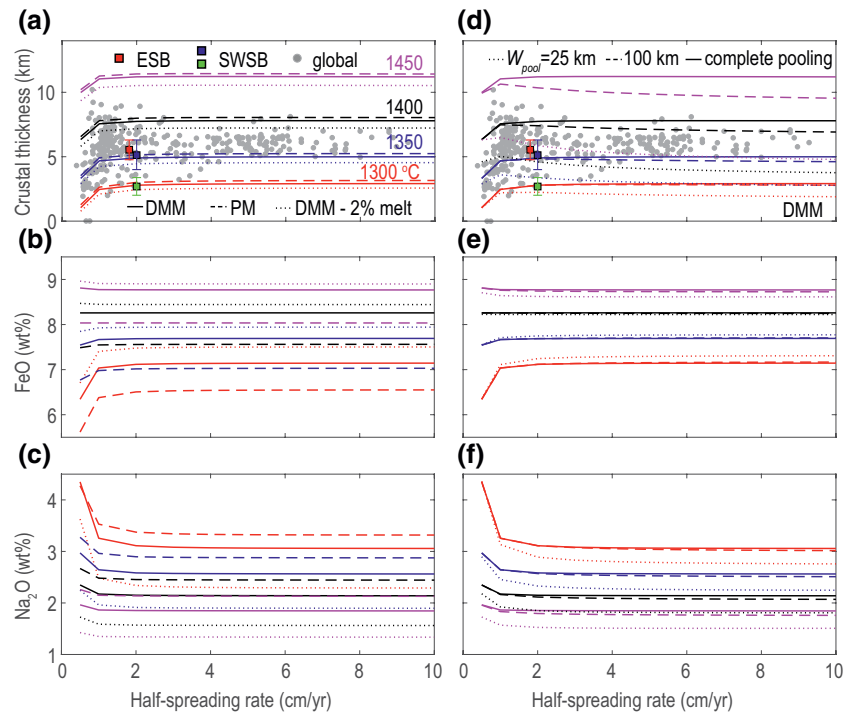
Figure 4. Predicted crustal thickness, FeO, and Na$_2$O contents in the aggregate melt as a function of half-spreading rate, mantle potential temperature, mantle source composition, and melt pooling width. In panels a–c, a complete melt pooling width is assumed, while in panels d–f, the mantle source is set as the depleted MORB mantle. Complete pooling means that all the melt generated in the melt zone is transported and aggregated beneath the ridge axis. The red square represents the crustal thickness derived from OBS seismic profiles in the east subbasin (P1; Zhao et al., 2018) and the blue square represents the crustal thickness of the southwest subbasin (OBS973-1; Qiu et al., 2011). The green square represents the crustal thickness derived from multichannel seismic profile (Yu et al., 2018a). The small gray dots represent available seismically determined crustal thicknesses of global mid-ocean ridge segments (Chen, 1992; Dick et al., 2003; Harding et al., 2017; Jokat et al., 2003; White et al., 2001). ESB: east subbasin, SWSB: southwest subbasin, DMM: depleted MORB mantle (Workman & Hart, 2005), PM: primitive mantle (Hart & Zindler, 1986), DMM—2% melt: DMM depleted by 2% melt extraction (Behn & Grove, 2015).

melt fraction during the decompression melting process. In the BG15 model, the input mantle is described by a four-phase assemblage, (i.e., augite, orthopyroxene, olivine, and an aluminous phase, which is spinel or plagioclase depending on the pressure).

Table 2
End-Member Source Composition

End member	SiO$_2$	TiO$_2$	Al$_2$O$_3$	Cr$_2$O$_3$	FeO	MgO	CaO	K$_2$O	Na$_2$O
PM[a]	46.16	0.18	4.08	0.47	7.57	37.95	3.22	0.03	0.33
DMM[b]	44.82	0.13	3.99	0.57	8.20	38.82	3.18	0.01	0.28
Depleted DMM[c]	44.63	0.11	3.52	0.58	8.27	39.76	2.98	0.0003	0.15
LCC[d]	58.20	0.91	17.56	0	7.44	3.94	6.25	1.87	3.83

[a]Bulk primitive mantle (PM) of Hart and Zindler (1986) is renormalized without including MnO, NiO, CoO, and P$_2$O$_5$. [b]Bulk depleted MORB mantle (DMM) of Workman and Hart (2005) is renormalized without including MnO, NiO, and P$_2$O$_5$. [c]Bulk depleted DMM is calculated by removing 3% batch melt from the DMM of Workman and Hart (2005) at 10 kbar using the BG15 melting model (Behn & Grove, 2015). [d]Bulk lower continental crust (LCC) of Hacker et al. (2015) is renormalized without including MnO.

As mantle moves upward along a pressure-temperature path, the mantle temperature must be adjusted for the latent heat of melting. The latent heat of melting, which decreases the mantle temperature, is estimated by:

$$\Delta T = \frac{FL}{C_p} \tag{10}$$

where ΔT is temperature reduction, F is melt fraction, L is latent heat of melting, and C_p is specific heat capacity. Melting occurs when the corrected mantle temperature is higher than mantle solidus and continues until the temperature is below the solidus due to conductive cooling from the surface.

The mantle solidus ($T_{solidus}$) is pressure-dependent (Till et al., 2012). In the spinel stability field ($p \geq 9$ kbars), $T_{solidus}$ is given by:

$$T_{solidus} = 1212 + 11.99(p) - 97.33(1 - Mg\#) - 87.76(NaK\#) + 3.44(TiO_2) - 4.58(K_2O) \tag{11}$$

while in the plagioclase stability field ($p < 9$ kbars), $T_{solidus}$ is given by:

$$T_{solidus} = 1216 + 10.44(p) - 72.83(1 - Mg\#) - 194.9(NaK\#) + 24.08(TiO_2) - 1.55(K_2O) \tag{12}$$

where TiO_2 and K_2O are contents in the melt. The Mg and NaK numbers of the melt are defined by:

$$Mg\# = MgO/(MgO + FeO) \tag{13}$$

$$NaK\# = (Na_2O + K_2O)/(Na_2O + K_2O + CaO) \tag{14}$$

The content of oxides in the melt are estimated by the nonmodal batch melting equation:

$$C_m^i = \frac{C_0}{D_s^i + F\left(1 - P_m^i\right)} \tag{15}$$

where C_m^i is concentration of major element oxide (i) in the melt (m) at each melt step, C_0 is initial concentration, D_s^i is bulk partition coefficient of oxide (i) in solid phase (s), P_m^i is bulk partition coefficient of oxide (i) in melt (m), F is melt fraction.

3.2.2. Melt Migration

To estimate the aggregate melt composition and the resultant crustal thickness, it is important to determine the pattern of melt migration. We assume that the melt first percolates vertically upward through the mantle column until it encounters a permeability boundary (e.g., top of the melting region), then migrates laterally without further chemical interaction along this boundary and finally pools beneath the ridge axis (Ghods & Arkani-Hamed, 2000; Kelemen & Aharanov, 1998; Magde et al., 1997; Magde & Sparks, 1997; Sparks et al., 1993; Sparks & Parmentier, 1991). Compared to the solid mantle flow, the melt is assumed to migrate to the ridge axis instantaneously once it is generated. The most important factor controlling the total melt pooled beneath the ridge axis is how far the melt will migrate horizontally before it freezes in the mantle (i.e., the horizontal length scale for melt migration to the ridge axis). We test the effects of different melt pooling width (*Wpool*) on the crustal thickness and aggregate melt composition (Figure 4).

The aggregate melt composition beneath a spreading ridge is estimated by pooling all incremental melts within a distance of W_{pool} from the ridge axis and weighting them by the melt production rate (Behn & Grove, 2015). The crustal thickness is estimated by integrating the melt production rate of the concerned region and dividing by the spreading rate (Forsyth, 1993). The melt production rate is the integration of the melt productivity (*dF/dz*) and the mantle upwelling velocity over the area of the relevant model grid

(Figure 2c). The horizontal and vertical grid spacings are 1 km and 0.1 km, respectively. The equations are described by (Forsyth, 1993; Behn & Grove, 2015):

$$H = \frac{1}{2U} \iint \left[\frac{dF}{dz} u_z \right] dx dz \tag{16}$$

$$C_{\text{aggregate}}{}^i = \iint \left[\frac{C_m{}^i \frac{dF}{dz} u_z}{\iint \left[\frac{dF}{dz} u_z \right] dx dz} \right] dx dz \tag{17}$$

where F is melt fraction, z is depth, H is crustal thickness, U is half-spreading rate, u_z is vertical component of mantle flow velocity, $C_{aggregate}$ is the aggregate melt composition beneath the ridge axis, $C_m{}^i$ is concentration of major element oxide (i) in the melt (m) at each melting grid in the model domain.

3.3. Fractional Crystallization

Due to the cooling effect of shallow mantle lithosphere, the aggregate melt undergoes fractional crystallization before extraction at the ridge axis. To account for this process, we use the model of Yang et al. (1996), in which the fractional crystallization path (i.e., the liquid line of descent) was calculated as a function of melt composition and pressure between 0.001 and 10 kbars. We assume that the crystallization pressure corresponds to the depth where the melting ceases beneath the ridge axis based on our thermal model. We derive major element composition for each step of fractional crystallization, which allows us to compare the simulated melt composition to MORBs data corrected to the same MgO content (Behn & Grove, 2015; Gregg et al., 2009). For example, we calculate $Fe_{8.0}$ and $Na_{8.0}$ as the FeO and Na_2O content at an MgO content of 8.0 wt %. These commonly used geochemical proxies provide constraints on the depth ($Fe_{8.0}$) and extent ($Na_{8.0}$) of mantle melting (Klein & Langmuir, 1987).

The root mean square (RMS) of the differences between the predicted liquid line of decent (LLD) and the observed major element contents as calculated by the following, is used to constrain model parameters:

$$RMS = \sqrt{\frac{1}{N} \Sigma_{n=1}^{N} \left(X - X_L \right)^2} \tag{18}$$

where X is the observed major element content (e.g., FeO and Na_2O), X_L is the predicted major element content determined by the LLD at the same MgO value with X, and N is the total number of observations. Constrained by the observed crustal thickness and predicted LLDs, we then estimate the best fitting mantle potential temperature and mantle source composition of the study region.

4. Model Results

We calculate crustal thickness and major element content of the aggregate melt as a function of mantle potential temperature T_p, half-spreading rate U, mantle source composition, and melt pooling width W_{pool} (Figure 4). In this initial analysis, the fractional crystallization process of the aggregate melt is not considered. Among all the controlling parameters, mantle potential temperature has the greatest effect on the predicted crustal thickness and major element content (Figures 4a–4c). Increasing T_p produces a larger melt zone and greater total degree of melting (Figures 3e–3h), which results in systematically thicker crust, higher FeO, and lower Na_2O content of the aggregate melt (Figures 4a–4c). Half-spreading rate has a strong effect on the crustal thickness and major element content only when U is less than 2 cm/yr, especially for U of 0.5–1 cm/yr; the influence of half-spreading rate decreases with increasing mantle potential temperature (Figures 4a–4c).

To assess the influence of mantle source composition, we examine three mantle end-members including primitive mantle (PM) (Hart & Zindler, 1986), depleted MORB mantle (DMM) (Workman & Hart, 2005), and more depleted DMM (Behn & Grove, 2015). This later composition is created by extracting melt (e.g.,

2%) from the initial DMM composition using BG15 melting model. Mantle source composition has a small effect on the crustal thickness (Figure 4a). As the mantle solidus increases with increasing mantle depletion, the model with the PM source generates slightly thicker crust compared to the DMM and more depleted DMM sources (Workman & Hart, 2005). The aggregate melt composition is greatly affected by the initial mantle source composition (Figures 4b and 4c). Because of the relatively lower FeO and higher Na_2O content in the enriched PM composition (Table 2), the resulting aggregate melt has much lower FeO and higher Na_2O content compared to the DMM and more depleted DMM composition.

The effect of the melt pooling width W_{pool} on the crustal thickness is greater at higher mantle potential temperature and faster half-spreading rate (Figures 3 and 4d). The W_{pool} has a moderate influence on the aggregate melt chemistry (Figures 4e and 4f). The Na_2O content in the aggregate melt increases with increasing melt pooling width, because greater amount of off-axis melt with relatively higher Na_2O content (Figure 2d) pools beneath the ridge axis. However, the effect of W_{pool} on the FeO content is complex and dependent on mantle potential temperature (Figure 4e). The effect of W_{pool} is small when it is greater than 100 km (Figures 4d–4f).

4.1. Predicted Mantle Potential Temperature of the SCS Subbasins

We estimate the appropriate mantle potential temperature of the SCS to explain the observed crustal thickness. Considering the relatively small dependence of the crustal thickness on mantle source composition and wide melt pooling zone (more than 100 km) (Figure 4a), the models with DMM composition and W_{pool} of 100 km are set as reference cases for the following discussion. For the crustal thickness in the east subbasin (4.8–6.3 km), as derived from P wave velocity model, the required mantle potential temperature varies from 1,350 to 1,375 °C; meanwhile for the SW subbasin (4–6.3 km), the mantle potential temperature varies from 1,325 to 1,375 °C (Figure 4d).

4.2. Predicted Mantle Source Compositions of the SCS Subbasins

4.2.1. Single End-Member Source

We use the primitive mantle (PM) (Hart & Zindler, 1986), the depleted MORB mantle (DMM) (Workman & Hart, 2005), and a more depleted DMM (e.g., DMM—2% melt) (Behn & Grove, 2015), which have increasing degrees of mantle depletion, as starting mantle source compositions for the SCS (Figures 5 and S5). The PM model represents the average chemical composition of undepleted mantle after the segregation in Earth's core but before the extraction of continental crust, and the PM is assumed as the composition of the deep mantle (Hart & Zindler, 1986; Lyubetskaya & Korenaga, 2007; McDonough & Sun, 1995). The DMM model is the average source reservoir of MORBs, which has been depleted by 2–3% melt extraction compared to the PM (Workman & Hart, 2005). The more depleted DMM model is calculated by extracting a few percent of melt from the DMM composition (e.g., DMM—2% melt). As T_p increases, the FeO content in the aggregate melt increases (Figure 4b), and thus the predicted LLD of FeO moves upward (Figure 5a). While the Na_2O content in the aggregate melt decreases with increasing T_p (Figure 4c), the predicted LLD evolves downward (Figure 5b). As the assumed degree of prior melt extraction from the mantle source (i.e., the depletion degree of mantle source) increases, the FeO content increases (Figure 4b), but the Na_2O decreases (Figure 4c) at the same T_p. Thus, the predicted LLDs of FeO and Na_2O evolve in the opposite direction (Figure 5). W_{pool} has a relatively greater effect on the RMS values of the predicted LLD when W_{pool} is less than 100 km (Figures 6, and S6, S7).

For the east subbasin, the LLD predicted by the model with the DMM composition and mantle potential temperature of 1,350 °C explain most of the observed FeO and Na_2O contents (Figures 5a, 5b, and 6c). The appearance of plagioclase or augite in the melt would result in rapid decrease of Al_2O_3 and CaO contents (Gale et al., 2014). However, the CaO and Al_2O_3 contents of the SCS basalt samples do not show clear crystallization trends (Figure S5). Thus, the model parameters were mainly constrained by the FeO and Na_2O contents, which have relatively clear crystallization path (Figure 5). For models with the PM composition, the predicted LLD with T_p of 1,400 °C could fit a few observations of the east subbasin (Figures 5c and 5d). However, the predicted crustal thickness at the same T_p is much greater than seismically determined crustal
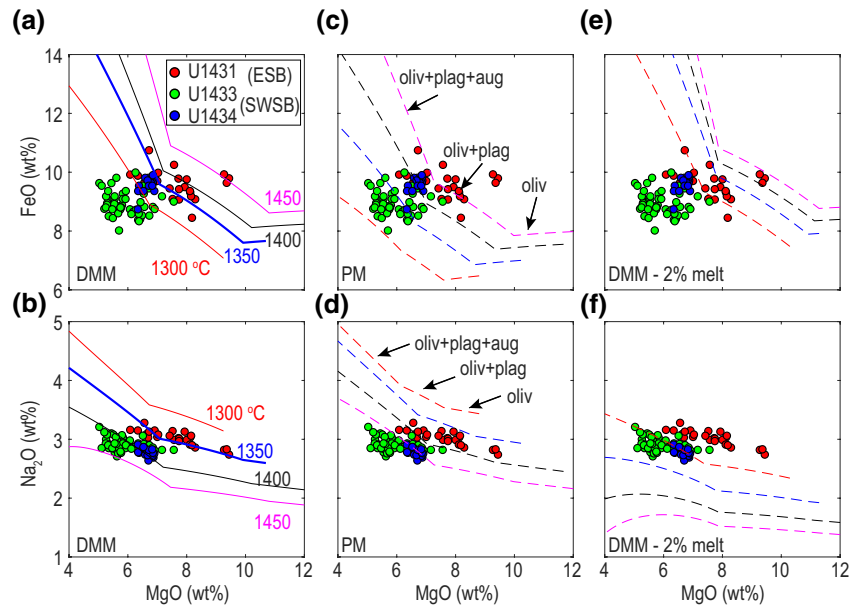
Figure 5. Calculated FeO and Na_2O versus MgO contents for models with different mantle source compositions and mantle potential temperatures. The observed FeO and Na_2O contents are selected from Zhang et al. (2018b). Site U1431 is located in the east subbasin, and sites U1433 and U1434 are located in the southwest subbasin. The crystallizing phases that correspond to changes in the liquid line of descent slope are marked in panels c and d. The half-spreading rate of 2 cm/yr and W_{pool} of 100 km are assumed in the models. Ol, olivine, plag, plagioclase, and aug, augite.

thickness (Figure 4a). Models with a more depleted DMM (DMM—2% melt) could not fit the observed crustal thickness, FeO, and Na_2O simultaneously (Figures 5e, 5f, and S7).

For the SW subbasin, models with single-source mantle for any combinations of T_p and W_{pool} can not fit the observed crustal thickness, FeO, and Na_2O simultaneously (Figures 5, 6 and S6, S7). For example, at T_p of 1,300 °C, the predicted LLD with the DMM composition fits most of the observed FeO of the SW subbasin (Figure 5a), while the LLD plots significantly above the observed Na_2O contents (Figure 5b).

4.2.2. Mixing of Two End-Member Sources

We further examine models with mixing of two end-member sources. Here the W_{pool} is set at 100 km, due to its small effect on the predicted crustal thickness and melt composition (Figures 4d–4f). For the east subbasin, entraining a small proportion of PM in the DMM source could also explain most of the observations (Figures 7a–7c). However, mixtures of PM and DMM mantle sources can not explain the FeO and Na_2O contents of basalt samples in the SW subbasin (Figures 7d–7f). To explain these compositional data from the SW subbasin, a more depleted DMM contaminated by a fraction of lower continental crust (Hacker et al., 2015) is required (Figures 8d–8f and S8f), indicating that a complex mantle source exists in the SW subbasin. By contrast, no contribution of lower continental crust is needed for the east subbasin (Figures 8a–8c). Moreover, models with a mixture of PM and LCC could not fit the observations in either the east or SW subbasin (Figure S9).

We then calculate the crystallization paths and estimate the $Fe_{8.0}$ and $Na_{8.0}$ values of the SCS subbasins (Figure 9). For the east subbasin, the DMM composition and a T_p of 1350 °C are assumed. The estimated $Fe_{8.0}$ and $Na_{8.0}$ of the east subbasin (site U1431) is 9.0 ± 0.7 and 2.9 ± 0.2, respectively, which are within the range of global mid-ocean ridge values (Figure 10). For the SW subbasin, a more depleted DMM (e.g., DMM—3% melt) contaminated by 3% LCC (Hacker et al., 2015), and T_p of 1,350 °C are assumed. The estimated $Fe_{8.0}$ and $Na_{8.0}$ of the SW subbasin (sites U1433 and U1434) is 7.6 ± 1.0 and 2.5 ± 0.35, respectively, which are lower than that of the global mid-ocean ridge values (Figure 10). The CaO, Al_2O_3, and Sr/Nd of MORBs in the SCS vary greatly and do not show clear crystallization trends (Figure S10). The predicted LLDs do

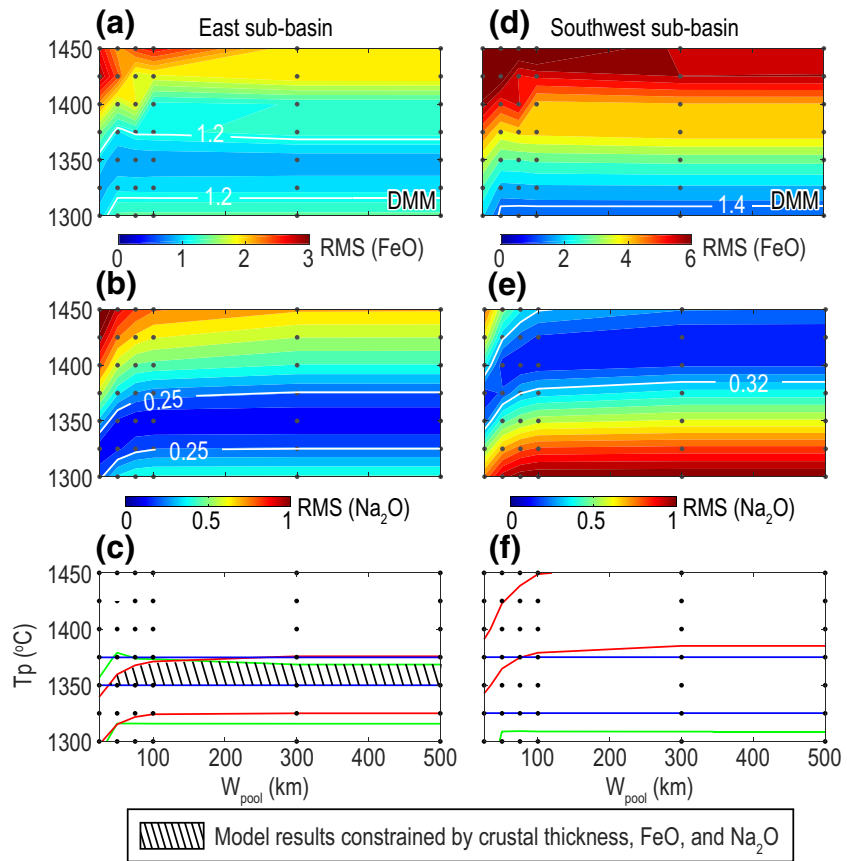**Figure 6.** Calculated root mean square (RMS) of the differences between the predicted liquid line of descent (LLD) and the observed FeO and Na$_2$O contents of the east (a–c) and southwest (d–f) subbasins as a function of melt pooling width W_{pool}. The acceptable RMS maximums (white contours) are constrained by the RMS of the predicted LLDs that fit the upper or lower limits of the observations (Figure 5). Due to greater variations in the FeO and Na$_2$O contents (Figure 5), the RMS maximum of the southwest subbasin is greater than that of the east subbasin. The areas covered with diagonal lines are the appropriate model solutions constrained by crustal thickness (blue lines), FeO (green lines), and Na$_2$O content (red lines). The small black dots indicate tested models with different mantle potential temperatures and melt pooling widths. The half-spreading rate is set as 2 cm/yr and the mantle source is assumed as the depleted MORB mantle.

not provide good fits to the observed CaO and Al$_2$O$_3$ variations. Moreover, we only consider the melting of spinel lherzolite, which is unable to explain the relatively lower CaO content of the east subbasin resulting from pyroxenite melting (Figure S10b) (Zhang et al., 2018b).

5. Discussion

5.1. Factors Controlling Crustal Thickness and Major Element Contents of the SCS

The predicted crustal thickness and major element geochemistry are greatly affected by mantle potential temperature, which controls the thermal structure beneath the ridge axis (Behn & Grove, 2015; Gregg et al., 2009). Mantle source compositions have relatively small effects on the predicted crustal thickness, but large influence on the major element geochemistry (Figures 4 and 10). Higher mantle potential temperature will result in higher Fe$_{8.0}$ and lower Na$_{8.0}$ as more melt is generated. Mantle depletion will lead to higher Fe$_{8.0}$, but lower Na$_{8.0}$ because of the expected increase in FeO and decrease in Na$_2$O in the mantle source (Table 2). The composition of lower continental crust (Hacker et al., 2015) is distinct from the depleted MORB mantle (Workman & Hart, 2005) or primitive mantle (Hart & Zindler, 1986), thus adding a fraction of LCC will greatly change the predicted Fe$_{8.0}$ and Na$_{8.0}$.
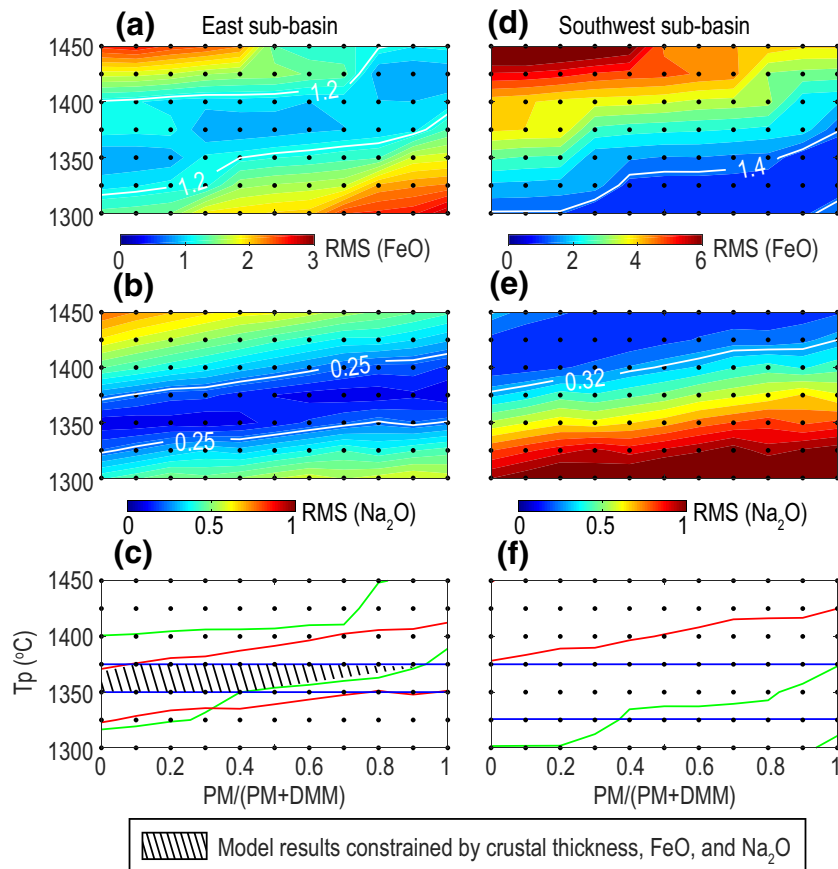
Figure 7. Calculated root mean square of the differences between the predicted liquid line of descent and the observed FeO and Na$_2$O contents for models with the DMM contaminated by different proportion of PM. The half-spreading rate of 2 cm/yr and melt pooling width of 100 km are assumed in the models.

Half-spreading rate only has a large influence the predicted crustal thickness and major element geochemistry when U is less than 2 cm/yr. In both of the SCS subbasins, the half-spreading rates are constant at about 2 cm/yr before the cessation of seafloor spreading (Li et al., 2014). However, a narrow zone with thin crust (<5 km) was observed in the east subbasin along the fossil spreading ridge through analyzing seismic profiles (Zhao et al., 2018). Furthermore, systematic variations in the basalt composition at sites U1433 and U1434 (Figure 1) indicate a decrease in the degree of mantle melting at these sites (Sun et al., 2020). These phenomena suggest that the half-spreading rate decreased as seafloor spreading ceased in the SCS; however, limited resolution in the magnetic anomalies do not allow us to formally test this hypothesis (Li et al., 2014). If we would assume an ultraslow spreading rate of 0.5 cm/yr, the required mantle potential temperatures in the east and SW subbasins would have increased by 25 °C (Figure 11).

The melt pooling width has a large effect on the predicted crustal thickness and major element geochemistry only when W_{pool} is less than 100 km. However, the lateral scale of melt migration beneath the spreading ridge is not well constrained. Gregg et al. (2009) used 3-D mid-ocean ridge models with W_{pool} of 75 km to simulate crustal thickness and major element variations observed at the Siqueiros transform fault. Using calculations of the crystallization rates at ridges with different spreading rates, Hebert and Montési (2010) proposed a strong permeability barrier beneath the ridge axis, which facilitates the buoyant melts to transport to the ridge axis. The predicted width of melt pooling increases with spreading rate and extends 20–160 km off axis for spreading rates ranging from 1 to 10 cm/yr. However, the Hebert and Montési (2010) model significantly underestimates the crustal thickness at ridges with half-spreading rate less than 2 cm/yr because of the narrow width of the permeability barrier (<50 km). They speculated that such difficulty may indicate a different lateral melt focusing mechanism at ultraslow spreading rates.
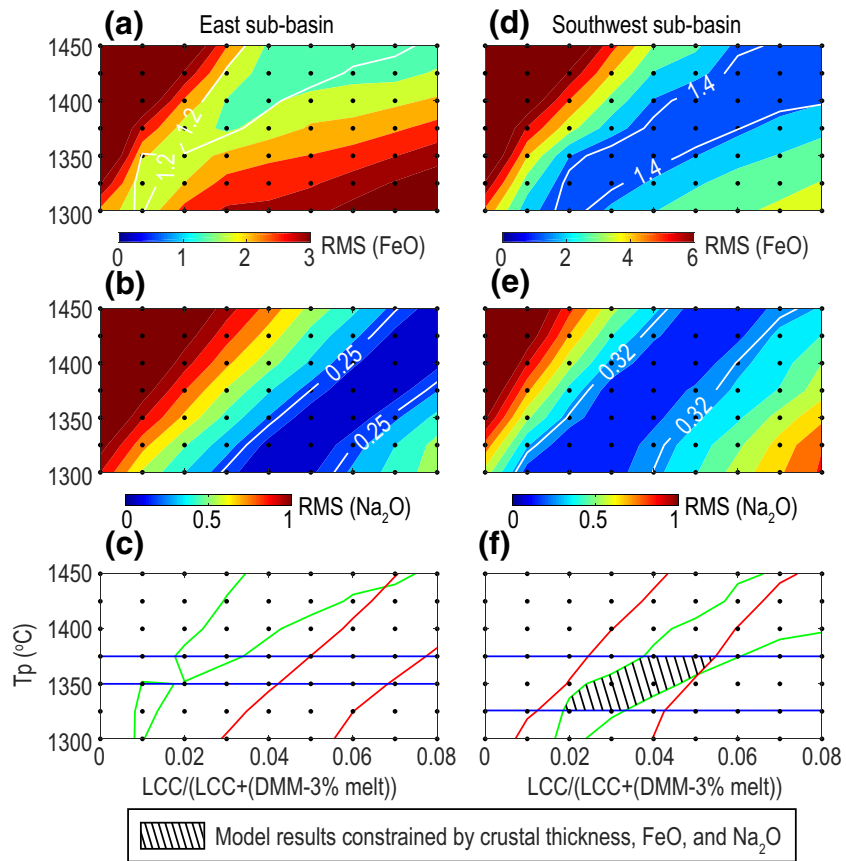
Figure 8. Calculated root mean square of the differences between the predicted liquid line of descent and the observed FeO and Na₂O contents for models with a more depleted DMM (e.g., DMM—3% melt) contaminated by a fraction of lower continental crust (LCC) (Hacker et al., 2015). The composition of the more depleted DMM is calculated by extracting 3% batch melt from the DMM. The half-spreading rate of 2 cm/yr and melt pooling width of 100 km are assumed in the models.

Although we assume W_{pool} of 100 km, the effective melt pooling width varies for different spreading rates (Figure 3). For models with half-spreading rate less than 1 cm/yr, W_{pool} of 100 km results in complete melt pooling (i.e., all generated melts contribute to crust creation) (Figures 3a and 3b). For models with narrow melt pooling, slightly higher mantle potential temperature is needed to explain the observed crustal thickness and basalt composition (Figure S11). Moreover, model results with W_{pool} of 100 km could well explain the observed crustal thickness and major element geochemistry of global mid-ocean ridge samples (Figure 12). Given the observed variations in the estimated mantle potential temperatures of the SCS, the half-spreading rate of 2 cm/yr and the melt pooling width of 100 km assumed in the study appear to be reasonable (Figures 11 and S11).

5.2. Mantle Potential Temperature and Source Composition of the SCS Subbasins

Constrained by the observed oceanic crustal thickness and basalt major element contents, we estimate mantle potential temperature and source composition of the SCS subbasins prior to the cessation of sea-floor spreading. For the east subbasin, the estimated mantle potential temperature varies in a range of 1,350–1,375 °C, which is comparable to that of normal mid-ocean ridges away from mantle plumes (Dalton et al., 2014). Given the half-spreading rate of 2 cm/yr in the east subbasin, a model with depleted MORB mantle and mantle potential temperature of 1,350–1,375 °C can explain most of the observations (Figure 11). A few percent of primitive mantle are allowed in the mantle source model of the east subbasin (Figure 7), indicating potential influence of deep mantle. The crystallization temperature of the primitive
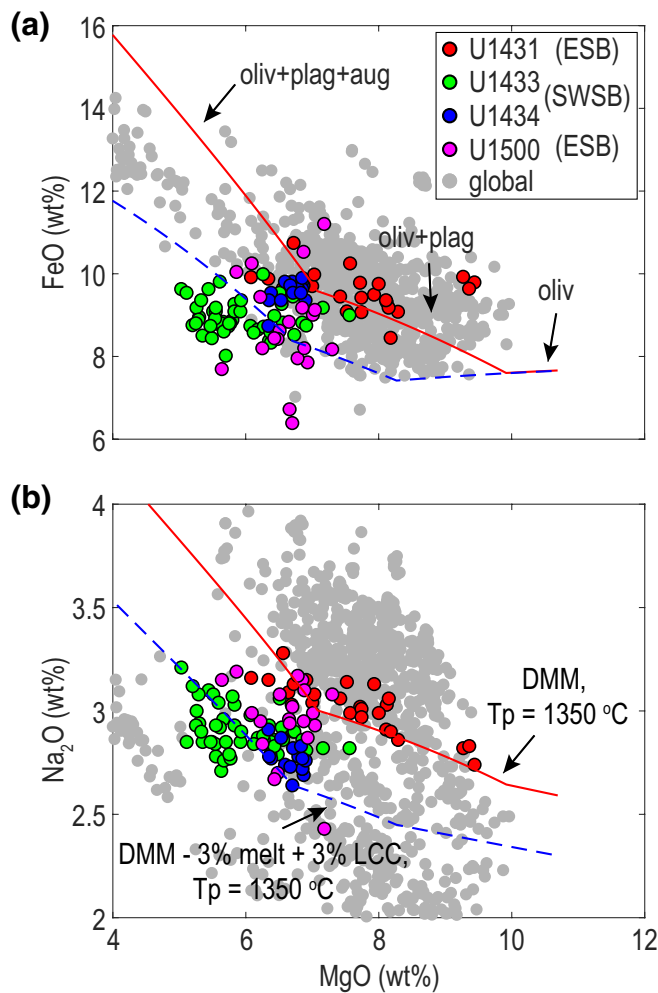
Figure 9. Liquid lines of descent calculated by the best fitting models of the east (red line) and southwest subbasins (blue dashed line). Site U1431 is located in the east subbasin, site U1500 is located at the northern margin of the east subbasin, and sites U1433 and U1434 are located in the southwest subbasin. The basalt compositions of IODP sites are selected from Zhang et al. (2018b) and Yu and Liu (2020). The gray dots represent global mid-ocean ridge basalt compositions for segments with half-spreading rate less than 4 cm/yr, which are modified from Gale et al. (2014). The half-spreading rate of 2 cm/yr and melt pooling width of 100 km are assumed in the models.

olivine at site U1431 is estimated to be 1,350 °C, which is much higher than that of the MORBs at normal mid-ocean ridges but comparable to that of the Iceland ocean island basalts (OIBs) (Yang et al., 2019), and this suggests the possibility of the influence of mantle plume on the SCS ridge magmatism at the east subbasin (Yang et al., 2019). The elevated Pb isotope composition of basalt samples from site U1431 could be explained by the influence of the Hainan mantle plume (Zhang et al., 2018b). However, the normal mantle potential temperature of 1,350–1,375 °C, oceanic crustal thickness of 5–6 km (Ruan et al., 2016; Zhao et al., 2018) are inconsistent with the existence of a large mantle plume that produced significantly thickened crust and uplifted topography (Campbell, 2007; Dordevic & Georgen, 2016; Ito et al., 2003).

Yang et al. (2019) proposed a model of revised eclogite-rich low buoyancy plume generated by subducting systems around the SCS area to explain these contradictions. Significantly lower bulk-rock CaO content of site U1431 basalts indicates that an eclogite/pyroxenite-rich component rising from a greater mantle depth could have contributed to the mantle source of the east subbasin (Herzberg & Asimow, 2008; Zhang et al., 2018b). Such lower bulk-rock CaO content can not be explained by our models assuming only melting of spinel lherzolite (Figure S10). Moreover, the estimated crustal thickness, $Fe_{8.0}$, and $Na_{8.0}$ of the east subbasin is comparable to that of the global mid-ocean ridge segments (Figure 12), implying that the SCS east subbasin samples are produced at a similar spreading regime as at mature mid-ocean ridges. Thus, we assume that the mantle source in the east subbasin prior to the cessation of seafloor spreading is mainly composed of the depleted MORB mantle, and is slightly contaminated by subduction-related component (Yang et al., 2019; Zhang et al., 2018b, 2018b).

For the SW subbasin, the estimated mantle potential temperature is 1,325–1,375 °C, but the mantle source is significantly different from that of the east subbasin. The best mantle source model of the SW subbasin is composed of the more depleted DMM mixed with a fraction (2–5%) of lower continental crust before the cessation of seafloor spreading (Figures 8–10). The depleted DMM is calculated by extracting fractional melting from the depleted MORB mantle source of Workman and Hart (2005), which is a global average of the MORB mantle source. The more depleted DMM of the SW subbasin may indicate a slight deviation from the global average DMM composition and/or a more complicated 3-D patterns of melt pooling (Behn & Grove, 2015; Magde & Sparks, 1997). Sr-Nd-Pb isotope compositions of MORBs from sites U1433 and U1434 reveal the influence of a minor proportion of lower continental crust on the subridge mantle source of the SW subbasin during the opening of the SCS (Zhang

et al., 2018b). The variation trends of Nb/Th and Ta/U values are relatively close to the lower continental crust (Figure 13), suggesting that the magma source is probably contaminated by lower continental crust (Sun et al., 2020). The major element compositions and REE patterns of basalt samples from site U1500 (Yu & Liu, 2020) at the northern margin of the east subbasin are comparable to that of sites U1433 and U1434 in the SW subbasin (Figures S1 and S2). The variation trends of Nb/Th and Ta/U ratios of U1500, which are not sensitive to fractional crystallization and could be used to reflect the origin of the mantle (Niu & Batiza, 1997), are also consistent with that of U1433 and U1434, revealing the influence of lower continental crust (Figure 13). Thus, we conclude that the subridge mantle beneath the east subbasin during the initial spreading stage was also modified by a fraction of lower continental crust.
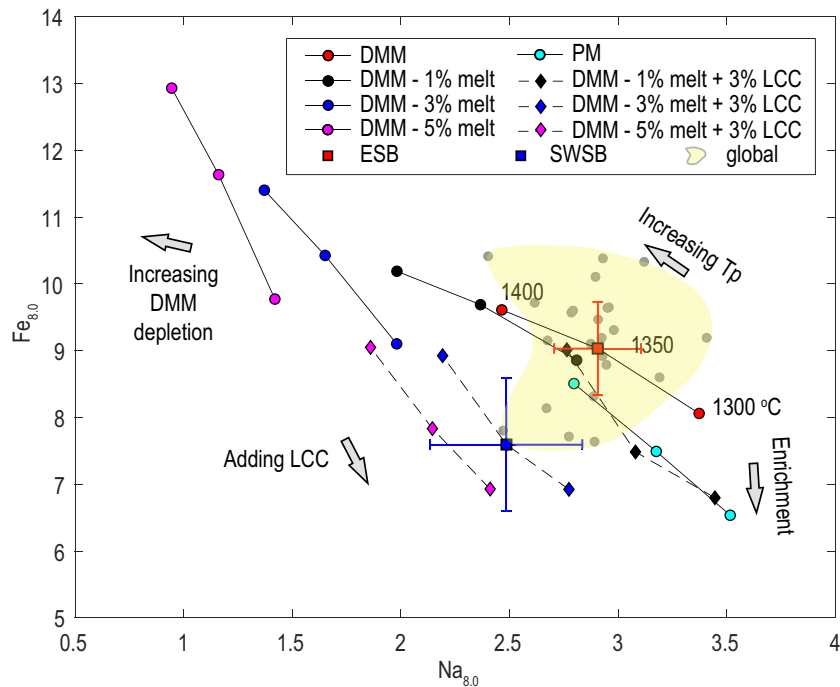
Figure 10. Predicted $Fe_{8.0}$ and $Na_{8.0}$ for models with different mantle source compositions and mantle potential temperatures. The squares are the estimated $Fe_{8.0}$ and $Na_{8.0}$ values of the east (red) and southwest subbasins (blue), respectively. The shaded yellow region with gray dots represents global $Fe_{8.0}$ and $Na_{8.0}$ for ridge segments with half-spreading rate varying from 1.5 to 2.5 cm/yr, which is modified from Gale et al. (2014).

5.3. Implications of Mantle Heterogeneity on the Mantle Evolution in the SCS

Mantle heterogeneity may play a major role in the SCS mantle evolution and melting (Sun et al., 2020; Yang et al., 2019; Zhang et al., 2018b, 2018c). Given the similar chemical compositions of U1500 with U1433 and U1434, which are different from that of U1431, it is proposed that the contribution of the lower continental crust to the subridge mantle melting decreases from the initial to mature spreading stage in the SCS (Figure 14).

The spreading regime at fossil ridges in the east and SW subbasin may represent different stages of mantle evolution in the SCS. Magnetic studies (Briais et al., 1993; Li et al., 2014; Taylor & Hayes, 1980) reveal that the seafloor spreading in the east subbasin has lasted for about 17–18 Ma (from ~32–33 to ~15 Ma), while
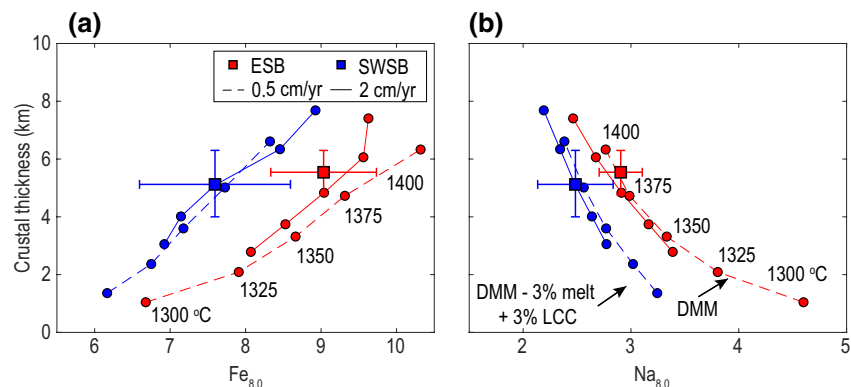

Figure 11. Predicted crustal thickness versus $Fe_{8.0}$ and $Na_{8.0}$ values for models with different half-spreading rates. The melt pooling width is set as 100 km.
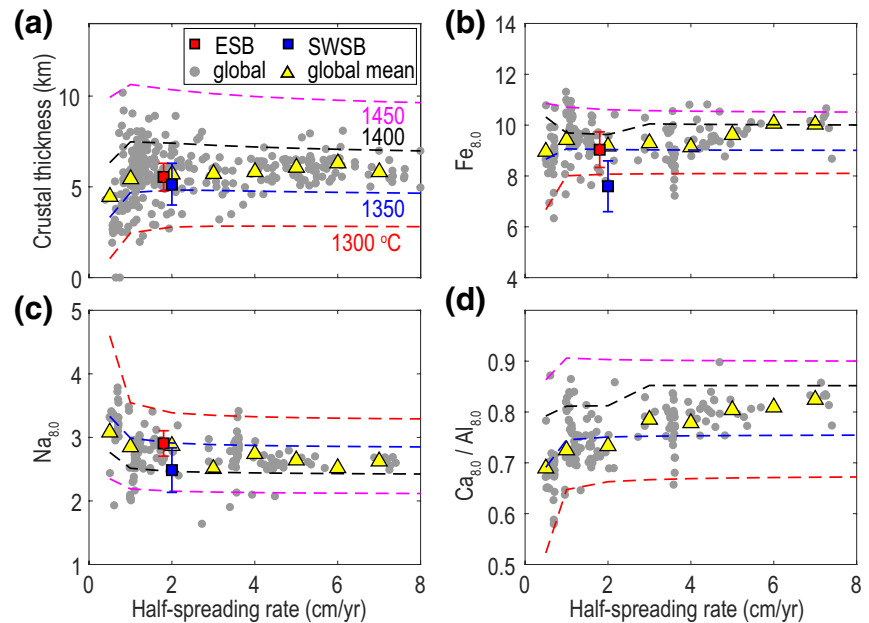
Figure 12. Comparison of crustal thickness and major element geochemistry of the SCS with global mid-ocean ridges. The available seismically determined crustal thickness of global mid-ocean ridge segments are selected from Chen (1992), White et al. (2001), Dick et al. (2003), Jokat et al. (2003), and Harding et al. (2017). The gray dots in panels b–d are individual segment averages selected from global MORB dataset of Gale et al. (2014) for segments away from the nearest hotspot by more than 750 km. The yellow triangles are the averages of global data binned in half-spreading rate of 1 cm/yr increment.

the SW subbasin experienced a significantly shorter spreading history of only 7–8 Ma (from ~23–24 to ~16 Ma). The convective upper mantle could be contaminated by the lower continental crust during continental rifting by crustal delamination (e.g., Escrig et al., 2004; Hanan et al., 2004; Jagoutz & Behn, 2013; Meyzen et al., 2005; Nishio et al., 2007; Regelous et al., 2009; Willbold & Stracke, 2010; Zhang et al., 2018b). As seafloor spreading continues, the contaminated mantle undergoes decompression melting and gradually moves away from the ridge axis, and the deeper unaltered mantle column moves upward and occupies the subridge mantle source region. This process would result in progressive decrease of the lower continental crust in the subridge mantle. We hypothesize that due to the relatively short spreading history, the lower
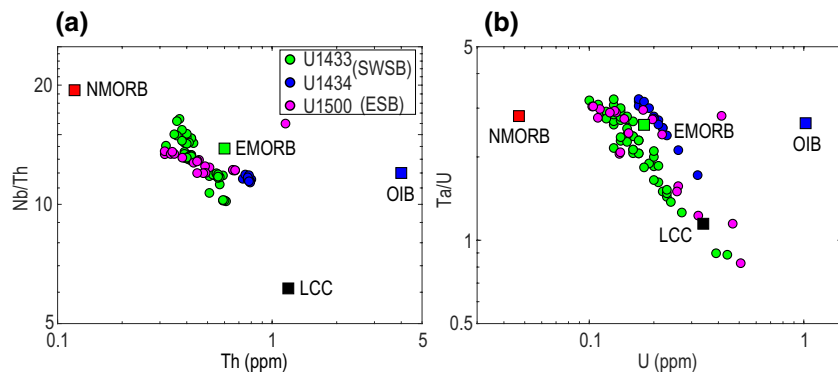

Figure 13. Comparison of Nb/Th versus Th (a) and Ta/U versus U (b) for basalt samples of sites U1433 and U1434 with site U1500. The bulk-rock trace element contents of site U1500 are selected from Yu and Liu (2020). Site U1500 is located at the northern margin of the east subbasin, and sites U1433 and U1434 are located near the fossil spreading ridge in the southwest subbasin Trace element contents of N-MORB, E-MORB, and OIB are from Sun and McDonough (1989). Trace element abundances of LCC are from Hacker et al. (2015).
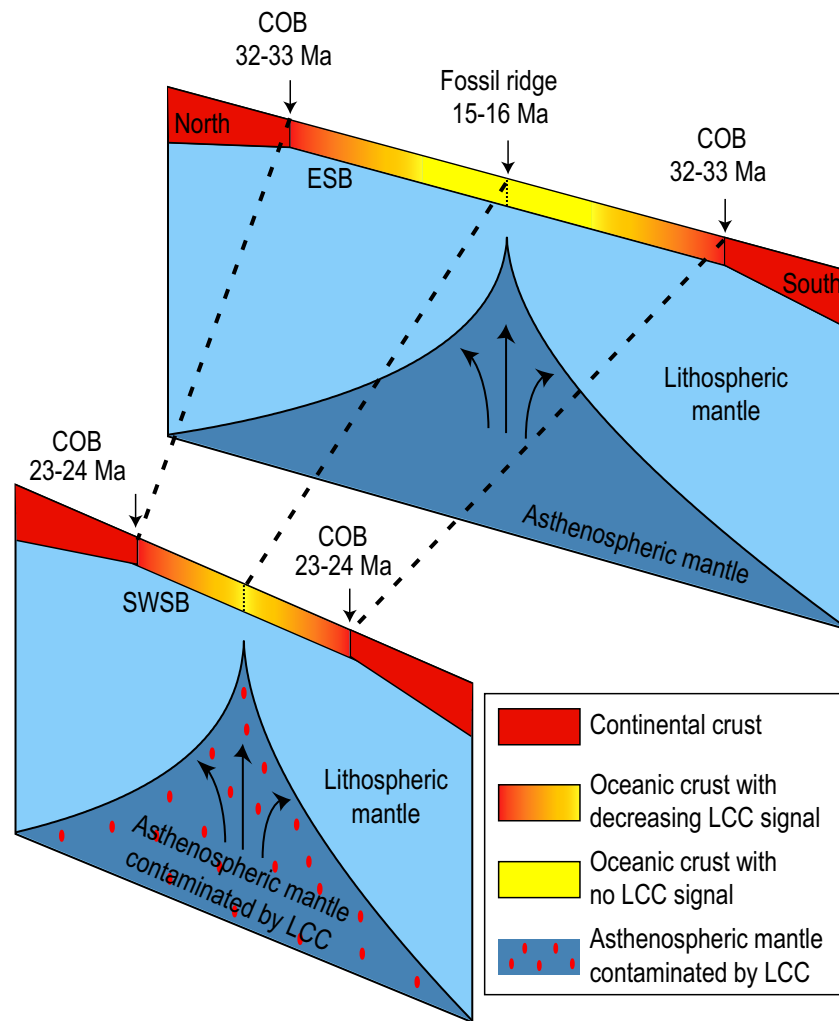
Figure 14. Conceptual models illustrating mantle source evolution during the period of seafloor spreading in the SCS subbasins. ESB: east subbasin; SWSB: southwest subbasin; COB: continent-ocean boundary; LCC: lower continental crust.

continental crust signal is still retained in the basalt samples of the SW subbasin ridge axis. However, the subridge mantle source composition and mantle melting processes are complex of the SCS and thus more detailed geophysical and geochemical studies should be conducted to reveal mantle evolution of the SCS.

6. Conclusions

Constrained by the seismically determined crustal thickness and the major element composition of the basalts sampled near fossil spreading centers in the SCS, we conduct computational geodynamic models to constrain mantle potential temperature and mantle source composition beneath the SCS subbasins, yielding the following main conclusions:

(1) The mantle potential temperatures of the east and SW subbasins are comparable.

(2) The mantle source compositions of the SCS subbasins have distinct differences. For the east subbasin, the subridge mantle source before the cessation of seafloor spreading is mainly composed of the depleted MORB mantle and the mantle source may be contaminated by small amounts of subduction-related eclogite/pyroxenite components. For the SW subbasin, a fraction of the lower continental crust appears

to have played an important role in the magma source, resulting in relatively lower $Fe_{8.0}$ and $Na_{8.0}$ values compared to the east subbasin.

(3) Basalt samples of site U1500 shows similar chemical compositions as that of U1433 and U1434, implying that the influence of the lower continental crust is maximum during the initial seafloor spreading and decreases as the ridge melts become more steady state.

References

Ahern, J., & Turcotte, D. (1979). Magma migration beneath an ocean ridge. *Earth and Planetary Science Letters*, *45*(1), 115–122. https://doi.org/10.1016/0012-821X(79)90113-4.

Asimow, P. D., Dixon, J., & Langmuir, C. (2004). A hydrous melting and fractionation model for mid-ocean ridge basalts: Application to the Mid-Atlantic Ridge near the Azores. *Geochemistry, Geophysics, Geosystems*, *5*, Q01E16. https://doi.org/10.1029/2003GC000568

Asimow, P. D., Hirschmann, M. M., & Stolper, E. (2001). Calculation of peridotite partial melting from thermodynamic models of minerals and melts, IV. Adiabatic decompression and the composition and mean properties of mid-ocean ridge basalts. *Journal of Petrology*, *42*(5), 963–998. https://doi.org/10.1093/petrology/42.5.963

Asimow, P. D., & Langmuir, C. H. (2003). The importance of water to oceanic mantle melting regimes. *Nature*, *421*(6925), 815–820. https://doi.org/10.1038/nature01429

Behn, M. D., Boettcher, M. S., & Hirth, G. (2007). Thermal structure of oceanic transform faults. *Geology*, *35*(4), 307–310. https://doi.org/10.1130/G23112A.1

Behn, M. D., & Grove, T. L. (2015). Melting systematics in mid-ocean ridge basalts: Application of a plagioclase-spinel melting model to global variations in major element chemistry and crustal thickness. *Journal of Geophysical Research*, *120*, 4863–4886. https://doi.org/10.1002/2015JB011885

Briais, A., Patriat, P., & Tapponnier, P. (1993). Updated interpretation of magnetic anomalies and seafloor spreading stages in the South China Sea: Implications for the Tertiary tectonics of Southeast Asia. *Journal of Geophysical Research*, *98*(B4), 6299–6328. https://doi.org/10.1029/92JB02280

Campbell, I. H. (2007). Testing the plume theory. *Chemical Geology*, *241*(3–4), 153–176. https://doi.org/10.1016/j.chemgeo.2007.01.024

Cande, S. C., & Kent, D. V. (1995). Revised calibration of the geomagnetic polarity timescale for the Late Cretaceous and Cenozoic. *Journal of Geophysical Research*, *100*(B4), 6093–6095. https://doi.org/10.1029/94JB03098

Chen, Y. J. (1992). Oceanic crustal thickness versus spreading rate. *Geophysical Research Letters*, *19*(8), 753–756. https://doi.org/10.1029/92GL00161

Chen, Y. J., & Morgan, W. J. (1990). A nonlinear rheology model for mid-ocean ridge axis topography. *Journal of Geophysical Research*, *95*(B11), 17583–17604. https://doi.org/10.1029/JB095iB11p17583

Childress, L., & the Expedition 368X Scientists (2019). *Expedition 368X Preliminary Report: South China Sea Rifted Margin*, College Station, TX: International Ocean Discovery Program. https://doi.org/10.14379/iodp.pr.368X.2019

Dalton, C. A., Langmuir, C. H., & Gale, A. (2014). Geophysical and geochemical evidence for deep temperature variations beneath mid-ocean ridges. *Science*, *344*(6179), 80–83. https://doi.org/10.1126/science.1249466

Dick, H. J., Lin, J., & Schouten, H. (2003). An ultraslow-spreading class of ocean ridge. *Nature*, *426*(6965), 405–412. https://doi.org/10.1038/nature02128

Ding, W., Sun, Z., Dadd, K., Fang, Y., & Li, J. (2018). Structures within the oceanic crust of the central South China Sea basin and their implications for oceanic accretionary processes. *Earth and Planetary Science Letters*, *488*, 115–125. https://doi.org/10.1016/j.epsl.2018.02.011

Dordevic, M., & Georgen, J. (2016). Dynamics of plume-triple junction interaction: Results from a series of three-dimensional numerical models and implications for the formation of oceanic plateaus. *Journal of Geophysical Research*, *121*, 1316–1342. https://doi.org/10.1002/2014JB011869

Escrig, S., Capmas, F., Dupré, B., & Allègre, C. (2004). Osmium isotopic constraints on the nature of the DUPAL anomaly from Indian mid-ocean-ridge basalts. *Nature*, *431*(7004), 59–63. https://doi.org/10.1038/nature02904

Expedition 349 Scientists (2014). *Expedition 349 Preliminary Report: South China Sea tectonics: Opening of the South China Sea and its implications for southeast Asian tectonics, climates, and deep mantle processes since the late Mesozoic*. College Station, TX: International Ocean Discovery Program. https://doi.org/10.14379/iodp.pr.349.2014

Fan, W., & Menzies, M. (1992). Destruction of aged lower lithosphere and accretion of asthenosphere mantle beneath eastern China. *Geotectonics and Metallogeny*, *16*, 171–180.

Forsyth, D. W. (1993). Crustal thickness and the average depth and degree of melting in fractional melting models of passive flow beneath mid-ocean ridges. *Journal of Geophysical Research*, *98*(B9), 16073–16079. https://doi.org/10.1029/93JB01722

Gale, A., Langmuir, C. H., & Dalton, C. A. (2014). The global systematics of ocean ridge basalts and their origin. *Journal of Petrology*, *55*(6), 1051–1082. https://doi.org/10.1093/petrology/egu017

Georgen, J. E. (2011). Lithospheric control on the spatial pattern of Azores hotspot seafloor anomalies: Constraints from a model of plume-triple junction interaction. *Geophysical Research Letters*, *38*, L19305. https://doi.org/10.1029/2011GL048742

Georgen, J. E. (2014). Interaction of a mantle plume and a segmented mid-ocean ridge: Results from numerical modeling. *Earth and Planetary Science Letters*, *392*, 113–120. https://doi.org/10.1016/j.epsl.2014.01.035

Ghods, A., & Arkani-Hamed, J. (2000). Melt migration beneath mid-ocean ridges. *Geophysical Journal International*, *140*(3), 687–697. https://doi.org/10.1046/j.1365-246X.2000.00032.x

Gregg, P. M., Behn, M. D., Lin, J., & Grove, T. L. (2009). Melt generation, crystallization, and extraction beneath segmented oceanic transform faults. *Journal of Geophysical Research*, *114*, B11102. https://doi.org/10.1029/2008JB006100

Grove, T. L., Kinzler, R. J., & Bryan, W. B. (1992). Fractionation of mid-ocean ridge basalt (MORB). In J. P. Morgan, D. K. Blackman, & J. M. Sinton (Eds.), Mantle flow and melt generation at mid-ocean ridges geophysical Monograph series (Vol. 71, pp. 281–310). Washington, DC: American Geophysical Union.

Hacker, B. R., Kelemen, P. B., & Behn, M. D. (2015). Continental lower crust. *Annual Review of Earth and Planetary Sciences*, *43*, 167–205. https://doi.org/10.1146/annurev-earth-050212-124117

Hanan, B. B., Blichert-Toft, J., Pyle, D. G., & Christie, D. M. (2004). Contrasting origins of the upper mantle revealed by hafnium and lead isotopes from the Southeast Indian Ridge. *Nature*, *432*(7013), 91–94. https://doi.org/10.1038/nature03026

Harding, J. L., Van Avendonk, H. J., Hayman, N. W., Grevemeyer, I., Peirce, C., & Dannowski, A. (2017). Magmatic-tectonic conditions for hydrothermal venting on an ultraslow-spread oceanic core complex. *Geology*, *45*(9), 839–842.

Hart, S. R., & Zindler, A. (1986). In search of a bulk-Earth composition. *Chemical Geology*, *57*(3–4), 247–267. https://doi.org/10.1016/0009-2541(86)90053-7

Hebert, L. B., & Montési, L. G. (2010). Generation of permeability barriers during melt extraction at mid-ocean ridges. *Geochemistry, Geophysics, Geosystems*, *11*, Q12008. https://doi.org/10.1029/2010GC003270

Herzberg, C., & Asimow, P. D. (2008). Petrology of some oceanic island basalts: PRIMELT2.XLS software for primary magma calculation. *Geochemistry, Geophysics, Geosystems*, *9*, Q09001. https://doi.org/10.1029/2008GC002057

Huang, J. (2014). P-and S-wave tomography of the Hainan and surrounding regions: Insight into the Hainan plume. *Tectonophysics*, *633*, 176–192. https://doi.org/10.1016/j.tecto.2014.07.007

Ito, G., Lin, J., & Graham, D. (2003). Observational and theoretical studies of the dynamics of mantle plume-mid-ocean ridge interaction. *Reviews of Geophysics*, *41*(4), 1017. https://doi.org/10.1029/2002RG000117

Jagoutz, O., & Behn, M. D. (2013). Foundering of lower island-arc crust as an explanation for the origin of the continental Moho. *Nature*, *504*, 131–134. https://doi.org/10.1038/nature12758

Jian, Z., Larsen, H. C., Alvarez Zarikian, C. A., & the Expedition 368 Scientists (2018). *Expedition 368 Preliminary Report: South China Sea Rifted Margin*, College Station, TX: International Ocean Discovery Program. https://doi.org/10.14379/iodp.pr.368.2018

Jokat, W., Ritzmann, O., Schmidt-Aursch, M. C., Drachev, S., Gauger, S., & Snow, J. (2003). Geophysical evidence for reduced melt production on the Arctic ultraslow Gakkel mid-ocean ridge. *Nature*, *423*(6943), 962. https://doi.org/10.1038/nature01706

Katz, R. F., Spiegelman, M., & Langmuir, C. H. (2003). A new parameterization of hydrous mantle melting. *Geochemistry, Geophysics, Geosystems*, *4*(9), 1073. https://doi.org/10.1029/2002GC000433

Kelemen, P. B., & Aharonov, E. (1998). Periodic formation of magma fractures and generation of layered gabbros in the lower crust beneath oceanic spreading ridges. In W. R. Buck, P. T. Delaney, J. A. Karson, & Y. Lagabrielle (Eds.), Faulting and magmatism at mid-ocean ridges, geophysical Monograph series (Vol. 106, pp. 267–290). Washington, DC: American Geophysical Union.

Kinzler, R. J. (1997). Melting of mantle peridotite at pressures approaching the spinel to garnet transition: Application to mid-ocean ridge basalt petrogenesis. *Journal of Geophysical Research*, *102*(B1), 853–874. https://doi.org/10.1029/96JB00988

Kinzler, R. J., & Grove, T. L. (1992a). Primary magmas of mid-ocean ridge basalts. 1: Experiments and methods. *Journal of Geophysical Research*, *97*(B5), 6885–6906. https://doi.org/10.1029/91JB02840

Kinzler, R. J., & Grove, T. L. (1992b). Primary magmas of mid-ocean ridge basalts. 2: Applications. *Journal of Geophysical Research*, *97*(B5), 6907–6926. https://doi.org/10.1029/91JB02841

Kinzler, R. J., & Grove, T. L. (1993). Corrections and further discussion of the primary magmas of mid-ocean ridge basalts, 1 and 2. *Journal of Geophysical Research*, *98*(B12), 22339–22347. https://doi.org/10.1029/93JB02164

Klein, E. M., & Langmuir, C. H. (1987). Global correlations of ocean ridge basalt chemistry with axial depth and crustal thickness. *Journal of Geophysical Research*, *92*(B8), 8089–8115. https://doi.org/10.1029/JB092iB08p08089

Langmuir, C. H., Klein, E. M., & Plank, T. (1992). Petrological systematics of mid-ocean ridge basalts: Constraints on melt generation beneath ocean ridges. In J. P. Morgan, D. K. Blackman, & J. M. Sinton (Eds.), Mantle flow and melt generation at mid-ocean ridges geophysical Monograph series (Vol. 71, pp. 183–280). Washington, DC: American Geophysical Union.

Larsen, H. C., Mohn, G., Nirrengarten, M., Sun, Z., Stock, J., Jian, Z., et al. (2018). Rapid transition from continental breakup to igneous oceanic crust in the South China Sea. *Nature Geoscience*, *11*(10), 782–789. https://doi.org/10.1038/s41561-018-0198-1

Li, J., Ding, W., Wu, Z., Zhang, J., & Dong, C. (2012). The propagation of seafloor spreading in the southwestern subbasin, South China Sea. *Science Bulletin*, *57*(24), 3182–3191. https://doi.org/10.1007/s11434-012-5329-2

Li, C., Li, J., Ding, W., Franke, D., Yao, Y., Shi, H., et al. (2015). Seismic stratigraphy of the central South China Sea basin and implications for neotectonics. *Journal of Geophysical Research*, *120*, 1377–1399. https://doi.org/10.1002/2014JB011686

Lin, J., Xu, Y., Sun, Z., & Zhou, Z. (2019). Mantle upwelling beneath the South China Sea and links to surrounding subduction systems. *National Science Review*, *6*(5), 877–881. https://doi.org/10.1093/nsr/nwz123

Lissenberg, C. J., & Dick, H. J. (2008). Melt-rock reaction in the lower oceanic crust and its implications for the genesis of mid-ocean ridge basalt. *Earth and Planetary Science Letters*, *271*(1–4), 311–325. https://doi.org/10.1016/j.epsl.2008.04.023

Li, C., Xu, X., Lin, J., Sun, Z., Zhu, J., Yao, Y., et al. (2014). Ages and magnetic structures of the South China Sea constrained by deep tow magnetic surveys and IODP Expedition 349. *Geochemistry, Geophysics, Geosystems*, *15*, 4958–4983. https://doi.org/10.1002/2014GC005567

Lyubetskaya, T., & Korenaga, J. (2007). Chemical composition of Earth's primitive mantle and its variance: 1. Method and results. *Journal of Geophysical Research*, *112*, B03211. https://doi.org/10.1029/2005JB004223

Magde, L. S., & Sparks, D. W. (1997). Three-dimensional mantle upwelling, melt generation, and melt migration beneath segment slow spreading ridges. *Journal of Geophysical Research*, *102*(B9), 20571–20583. https://doi.org/10.1029/97JB01278

Magde, L. S., Sparks, D. W., & Detrick, R. S. (1997). The relationship between buoyant mantle flow, melt migration, and gravity bull's eyes at the Mid-Atlantic Ridge between 33° N and 35° N. *Earth and Planetary Science Letters*, *148*(1–2), 59–67. https://doi.org/10.1016/S0012-821X(97)00039-3

McDonough, W. F., & Sun, S.-S. (1995). The composition of the Earth. *Chemical Geology*, *120*(3–4), 223–253. https://doi.org/10.1016/0009-2541(94)00140-4.

Meyzen, C. M., Ludden, J. N., Humler, E., Luais, B., Toplis, M. J., Mével, C., & Storey, M. (2005). New insights into the origin and distribution of the DUPAL isotope anomaly in the Indian Ocean mantle from MORB of the Southwest Indian Ridge. *Geochemistry, Geophysics, Geosystems*, *6*, Q11K11. https://doi.org/10.1029/2005GC000979

Mondy, L. S., Rey, P. F., Duclaux, G., & Moresi, L. (2018). The role of asthenospheric flow during rift propagation and breakup. *Geology*, *46*(2), 103–106. https://doi.org/10.1130/G39674.1.

Montési, L. G. J., Behn, M. D., Hebert, L. B., Lin, J., & Barry, J. L. (2011). Controls on melt migration and extraction at the ultraslow Southwest Indian Ridge 10°-16° E. *Journal of Geophysical Research*, *116*, B10102. https://doi.org/10.1029/2011JB008259

Nishio, Y., Nakai, S. i., Ishii, T., & Sano, Y. (2007). Isotope systematics of Li, Sr, Nd, and volatiles in Indian Ocean MORBs of the Rodrigues Triple Junction: Constraints on the origin of the DUPAL anomaly. *Geochimica et Cosmochimica Acta*, *71*(3), 745–759. https://doi.org/10.1016/j.gca.2006.10.004

Niu, Y., & Batiza, R. (1997). Trace element evidence from seamounts for recycled oceanic crust in the Eastern Pacific mantle. *Earth and Planetary Science Letters*, *148*(3–4), 471–483. https://doi.org/10.1016/S0012-821X(97)00048-4

Ogg, J. G. (2012). Geomagnetic polarity time scale. In F. M. Gradstein, J. G. Ogg, M. D. Schmitz, & G. M. Ogg (Eds.), The geologic time scale (pp. 85–113). Boston, MA:Elsevier.

Paquet, M., Cannat, M., Brunelli, D., Hamelin, C., & Humler, E. (2016). Effect of melt/mantle interactions on MORB chemistry at the eastern-most Southwest Indian Ridge (61°–67° E). *Geochemistry, Geophysics, Geosystems*, *17*, 4605–4640. https://doi.org/10.1002/2016GC006385

Park, C. H., Tamaki, K., & Kobayashi, K. (1990). Age-depth correlation of the Philippine Sea back-arc basins and other marginal basins in the world. *Tectonophysics*, *181*(1–4), 351–371. https://doi.org/10.1016/0040-1951(90)90028-7

Pautot, G., Rangin, C., Briais, A., Wu, J., Han, S., Li, H., et al. (1990). The axial ridge of the south china sea-a seabeam and geophysical survey. *Oceanologica Acta*, *13*(2), 129–143.

Pichot, T., Delescluse, M., Chamot-Rooke, N., Pubellier, M., Qiu, Y., Meresse, F., et al. (2014). Deep crustal structure of the conjugate margins of the SW South China Sea from wide-angle refraction seismic data. *Marine and Petroleum Geology*, *58*, 627–643. https://doi.org/10.1016/j.marpetgeo.2013.10.008

Qiu, X., Zhao, M., Ao, W., Lv, C., Hao, T., You, Q., et al. (2011). OBS survey and crustal structure of the Southwest Sub-basin and Nansha Block, South China Sea. *Chinese Journal of Geophysics*, *54*(6), 1009–1021. https://doi.org/10.1002/cjg2.1680

Regelous, M., Niu, Y., Abouchami, W., & Castillo, P. R. (2009). Shallow origin for South Atlantic Dupal Anomaly from lower continental crust: Geochemical evidence from the Mid-Atlantic Ridge at 26 S. *Lithos*, *112*(1–2), 57–72. https://doi.org/10.1016/j.lithos.2008.10.012

Roland, E., Behn, M. D., & Greg, H. (2010). Thermal-mechanical behavior of oceanic transform faults: Implications for the spatial distribution of seismicity. *Geochemistry, Geophysics, Geosystems*, *11*, Q07001. https://doi.org/10.1029/2010GC003034

Ruan, A., Wei, X., Niu, X., Zhang, J., Dong, C., Wu, Z., & Wang, X. (2016). Crustal structure and fracture zone in the Central Basin of the South China Sea from wide angle seismic experiments using OBS. *Tectonophysics*, *688*, 1–10. https://doi.org/10.1016/j.tecto.2016.09.022

Shimizu, K., Saal, A. E., Myers, C. E., Nagle, A. N., Hauri, E. H., Forsyth, D. W., et al. (2016). Two-component mantle melting-mixing model for the generation of mid-ocean ridge basalts: Implications for the volatile content of the Pacific upper mantle. *Geochimica et Cosmochimica Acta*, *176*, 44–80. https://doi.org/10.1016/j.gca.2015.10.033

Sibuet, J. C., Yeh, Y. C., & Lee, C. S. (2016). Geodynamics of the South China Sea. *Tectonophysics*, *692*, 98–119. https://doi.org/10.1016/j.tecto.2016.02.022

Sinton, J. M., & Detrick, R. S. (1992). Mid-ocean ridge magma chambers. *Journal of Geophysical Research*, *97*(B1), 197–216. https://doi.org/10.1029/91JB02508

Sparks, D. W., & Parmentier, E. (1991). Melt extraction from the mantle beneath spreading centers. *Earth and Planetary Science Letters*, *105*(4), 368–377. https://doi.org/10.1016/0012-821X(91)90178-K

Sparks, D. W., Parmentier, E., & Morgan, J. P. (1993). Three-dimensional mantle convection beneath a segmented spreading center: Implications for along-axis variations in crustal thickness and gravity. *Journal of Geophysical Research*, *98*(B12), 21977–21995. https://doi.org/10.1029/93JB02397

Sun, Z., Lin, J., Qiu, N., Jian, Z., Wang, P., Pang, X., et al. (2019). The role of magmatism in the thinning and breakup of the South China Sea continental margin. *National Science Review*, *6*(5), 871–876. https://doi.org/10.1093/nsr/nwz116

Sun, S. S., & McDonough, W. F. (1989). Chemical and isotopic systematics of oceanic basalts: Implications for mantle composition and processes. Geological Society, London, Special Publications, 42(1), 313–345. https://doi.org/10.1144/GSL.SP.1989.042.01.19

Sun, Z., Stock, J., Klaus, A., & the Expedition 367 Scientists (2018). *Expedition 367 Preliminary Report: South China Sea Rifted Margin*, College Station, TX: International Ocean Discovery Program. https://doi.org/10.14379/iodp.pr.367.2018

Sun, K., Wu, T., Liu, X., Chen, X. G., & Li, C. F. (2020). Lithogeochemistry of the mid-ocean ridge basalts near the fossil ridge of the southwest sub-basin, South China Sea. *Minerals*, *10*(5), 465. https://doi.org/10.3390/min10050465

Taylor, B., & Hayes, D. E. (1980). The tectonic evolution of the South China Basin. In D. E. Hayes (Ed.), The tectonic and geologic evolution of Southeast Asian seas and islands, Geophysical Monograph Series (Vol. 23, pp. 89–104). Washington, DC: American Geophysical Union.

Taylor, B., & Hayes, D. E. (1983). Origin and history of the South China Sea basin. In D. E. Hayes (Ed.), The tectonic and geologic evolution of Southeast Asian seas and islands: Part 2, geophysical Monograph series (Vol. 27, pp. 23–56). Washington, DC: American Geophysical Union.

Till, C., Grove, T., & Krawczynski, M. (2012). A melting model for variably metasomatized plagioclase and spinel lherzolite. *Journal of Geophysical Research*, *117*, B06206. https://doi.org/10.1029/2011JB009044

Tu, K., Flower, M. F. J., Carlson, R. W., Xie, G., Chen, C. Y., & Zhang, M. (1992). Magmatism in the South China Basin: 1. Isotopic and trace-element evidence for an endogenous Dupal mantle component. *Chemical Geology*, *97*(1–2), 47–63. https://doi.org/10.1016/0009-2541(92)90135-R

van Keken, P. E., Currie, C., King, S. D., Behn, M. D., Cagnioncle, A., He, J., et al. (2008). A community benchmark for subduction zone modeling. *Physics of the Earth and Planetary Interiors*, *171*(1–4), 187–197. https://doi.org/10.1016/j.pepi.2008.04.015

Wang, P., Huang, C. Y., Lin, J., Jian, Z., Sun, Z., & Zhao, M. (2019). The South China Sea is not a mini-Atlantic: plate-edge rifting vs intra-plate rifting. *National Science Review*, *6*(5), 902–913. https://doi.org/10.1093/nsr/nwz135

Wang, X., Wu, M., Liang, D., & Yin, A. (1985). Some geochemical characteristics of basalts in the South China Sea. *Geochemistry*, *4*(4), 380–390. https://doi.org/10.1007/BF02843275

Wei, S. S., & Chen, Y. J. (2016). Seismic evidence of the Hainan mantle plume by receiver function analysis in southern China. *Geophysical Research Letters*, *43*, 8978–8985. https://doi.org/10.1002/2016GL069513

White, R. S., Minshull, T. A., Bickle, M. J., & Robinson, C. J. (2001). Melt generation at very slow-spreading oceanic ridges: Constraints from geochemical and geophysical data. *Journal of Petrology*, *42*(6), 1171–1196. https://doi.org/10.1093/petrology/42.6.1171

Willbold, M., & Stracke, A. (2010). Formation of enriched mantle components by recycling of upper and lower continental crust. *Chemical Geology*, *276*(3), 188–197. https://doi.org/10.1016/j.chemgeo.2010.06.005

Workman, R. K., & Hart, S. R. (2005). Major and trace element composition of the depleted MORB mantle (DMM). *Earth and Planetary Science Letters*, *231*(1–2), 53–72. https://doi.org/10.1016/j.epsl.2004.12.005

Xu, Y., Wei, J., Qiu, H., Zhang, H., & Huang, X. (2012). Opening and evolution of the South China Sea constrained by studies on volcanic rocks: preliminary results and a research design. *Science Bulletin*, *57*(24), 3150–3164. https://doi.org/10.1007/s11434-011-4921-1

Yan, Q., Castillo, P., Shi, X., Wang, L., Liao, L., & Ren, J. (2015). Geochemistry and petrogenesis of volcanic rocks from Daimao Seamount (South China Sea) and their tectonic implications. *Lithos*, *218*, 117–126. https://doi.org/10.1016/j.lithos.2014.12.023

Yang, F., Huang, X. L., Xu, Y. G., & He, P. L. (2019). Plume-ridge interaction in the South China Sea: Thermometric evidence from Hole U1431E of IODP Expedition 349.*Lithos*, *324*, 466–478. https://doi.org/10.1016/j.lithos.2018.11.031

Yang, H. J., Kinzler, R. J., & Grove, T. L. (1996). Experiments and models of anhydrous, basaltic olivine-plagioclase-augite saturated melts from 0.001 to 10 kbar. *Contributions to Mineralogy and Petrology*, *124*(1), 1–18. https://doi.org/10.1007/s004100050169

Yan, Q., & Shi, X. (2007). Hainan mantle plume and the formation and evolution of the South China Sea. *Geological Journal of China Universities*, *13*(2), 311–322. https://doi.org/10.16108/j.issn1006-7493.2007.02.014

Yan, Q., Shi, X., & Castillo, P. R. (2014). The late Mesozoic-Cenozoic tectonic evolution of the South China Sea: A petrologic perspective. *Journal of Asian Earth Sciences*, *85*, 178–201. https://doi.org/10.1016/j.jseaes.2014.02.005

Yan, Q., Shi, X., Wang, K., Bu, W., & Xiao, L. (2008a). Major element, trace element, and Sr, Nd and Pb isotope studies of Cenozoic basalts from the South China Sea. *Science China Earth Sciences*, *51*(4), 550–566. https://doi.org/10.1007/s11430-008-0026-3

Yan, Q., Shi, X., Yang, Y., & Wang, K. (2008b). Potassium-argon/argon-40-argon-39 geochronology of Cenozoic alkali basalts from the South China Sea. *Acta Oceanologica Sinica*, *27*(6), 115–123.

Yu, J., Yan, P., Wang, Y., Zhang, J., Qiu, Y., Pubellier, M., & Delescluse, M. (2018a). Seismic Evidence for Tectonically Dominated Seafloor Spreading in the Southwest Sub-basin of the South China Sea. *Geochemistry, Geophysics, Geosystems*, *19*, 3459–3477. https://doi.org/10.1029/2018GC007819

Yu, M., Yan, Y., Huang, C. Y., Zhang, X., Tian, Z., Chen, W. H., & Santosh, M. (2018b). Opening of the South China Sea and upwelling of the Hainan plume. *Geophysical Research Letters*, *45*, 2600–2609. https://doi.org/10.1002/2017GL076872

Yu, X., & Liu, Z. (2020). Non-mantle-plume process caused the initial spreading of the South China Sea. *Scientific Reports*, *10*(1), 1–10. https://doi.org/10.1038/s41598-020-65174-y

Yu, Z., Li, J., Ding, W., Zhang, J., Ruan, A., & Niu, X. (2017). Crustal structure of the Southwest Subbasin, South China Sea, from wide-angle seismic tomography and seismic reflection imaging. *Marine Geophysical Research*, *38*(1–2), 85–104. https://doi.org/10.1007/s11001-016-9284-1

Zhang, F., Lin, J., Zhang, X., Ding, W., Wang, T., & Zhu, J. (2018a). Asymmetry in oceanic crustal structure of the South China Sea basin and its implications on mantle geodynamics. *International Geology Review*, *62*(7–8), 1–19. https://doi.org/10.1080/00206814.2018.1425922

Zhang, G., Luo, Q., Zhao, J., Jackson, M. G., Guo, L., & Zhong, L. (2018b). Geochemical nature of sub-ridge mantle and opening dynamics of the South China Sea. *Earth and Planetary Science Letters*, *489*, 145–155. https://doi.org/10.1016/j.epsl.2018.02.040

Zhang, G. L., Sun, W. D., & Seward, G. (2018c). Mantle source and magmatic evolution of the dying spreading ridge in the South China Sea. *Geochemistry, Geophysics, Geosystems*, *19*, 4385–4399. https://doi.org/10.1029/2018GC007570

Zhang, J., Li, J., Ruan, A., Wu, Z., Yu, Z., Niu, X., & Ding, W. (2016). The velocity structure of a fossil spreading center in the Southwest Sub-basin, South China Sea. *Geological Journal*, *51*(S1), 548–561. https://doi.org/10.1002/gj.2778

Zhao, M., He, E., Sibuet, J. C., Sun, L., Qiu, X., Tan, P., & Wang, J. (2018). Postseafloor spreading volcanism in the central east South China Sea and its formation through an extremely thin oceanic crust. *Geochemistry, Geophysics, Geosystems*, *19*, 621–641. https://doi.org/10.1002/2017GC007034

Zhao, M., Sibuet, J. C., & Wu, J. (2019). Intermingled fates of the South China Sea and Philippine Sea plate. *National Science Review*, *6*(5), 886–890. https://doi.org/10.1093/nsr/nwz107